Structural Behaviour of Folded Timber Sandwich Structures

Citation for published version:
Alqaryouti, Y, Fernando, D & Gattas, JM 2021, 'Structural Behaviour of Folded Timber Sandwich Structures', *Thin-Walled Structures*, vol. 169, 108345. https://doi.org/10.1016/j.tws.2021.108345

Digital Object Identifier (DOI):
10.1016/j.tws.2021.108345

Link:
Link to publication record in Edinburgh Research Explorer

Document Version:
Peer reviewed version

Published In:
Thin-Walled Structures

Structural Behaviour of Folded Timber Sandwich Structures

Yousef Alqaryouti[a], Dilum Fernando[a], Joseph M. Gattas[a,*]

[a]*School of Civil Engineering, University of Queensland, Australia*

Abstract

This paper aims to characterise the mechanical behaviour of folded timber sandwich structures developed using integral rotational press-fit (RPF) joints. Six folded arches are tested to failure, under three load cases designed to induce different sagging and hogging conditions at internal joints. Experimental testing showed failures occurring at joint locations with maximum hogging moment, with two failure types observed as FRP tensile and core compressive rupture. A nonlinear static analysis and simplified 2D frame model is proposed to predict moment distribution and failure load for FRP fracture modes. This model characterises the RPF joint as a nonlinear semi-rigid hinge, with assigned bilinear moment-curvature relation obtained from analysis of joint strain data collected during arch testing. Core compressive failures are shown to occur as an inelastic core buckling behaviour when there is misalignment between assembled core segments.

Keywords: digital fabrication, folded structures, modular construction, timber structures, integral joints, rotational stiffness, semi-rigid joints

1. Introduction

Folded plate structures are a type of self-supporting structural system composed exclusively of flat, segmented plates. Folded structures that use a simple unidirectional corrugation have been widely used historically due to their efficient load-carrying capabilities. Recent development however has

*Corresponding author

Email address: j.gattas@uq.edu.au (Joseph M. Gattas)

focused on folded structures with more complex geometric plate arrangements which can offer additional advantageous performance characteristics [1, 2, 3]. Deployable folded plate structures utilise folded plate arrangements with kinematic behaviours that allow for a very high speed of erection [4, 5, 6, 7]. Modular and prefabricated folded plate structures utilise repetitious or rationalised folded plate arrangements to introduce cost-effective manufacture and streamlined assembly [8, 9, 10].

Prefabricated folded plate structures have proven particularly effective when constructed from timber material, as timber has a rich history of joinery techniques suited for plate edge connections. Finger joints [11, 12], dovetail joints [13], box joints [14], bevel joints [15], and through-tenon joints [16, 17] are examples of carpentry techniques that have been successfully adapted for modern prefabrication. In each case, adaption has included algorithmic generation of component parts with timber joints included as integral mechanical attachments (IMAs); and subsequent manufacture of parts on computer-numerical controlled (CNC) machines. IMAs inherently streamline assembly as they eliminate the need for separate connector components, however this can be further improved with the incorporation of complex features through the algorithmic generation and CNC production process [18]. For example, press-fit joints constrain assembly of each part to a single direction of insertion and multiple tab-and-slot joints (MTSJs) introduce a self-locking feature that prevents disassembly of prior components in the assembly sequence [19, 20]

1.1. Folded structure performance characterisation

In all types of timber construction, connections are regarded as the critical structural design consideration. Connection strength will often dictate overall performance of the structural system and can govern member size, especially for tension or semi-rigid connections. As such, there has been a large research effort dedicated to characterising the mechanical attributes of IMAs and their impact on the overall structural behaviour of folded plate structures [21, 22]. Assembled folded plate arch structures with quadrilateral plates have been tested under central line loading for 3m and 6.5m spans [23, 24]; and structures with triangulated plates have been tested under distributed surface loading for 3m spans [19].

The use of IMAs allowed these assembled structures to achieve a high structural performance with use of a relatively thin Kerto-Q LVL material, just 21mm thick. However, ultimate failure still occurred at joint locations due to combined bending and shear loads induced from the double-corrugated folded geometries employed. Subsequent work in numerical modelling of these structures showed that the stiffness characteristics of folded arches are determined by the semi-rigid behaviours of plate edge connections [25, 26]. Related work has been completed to characterise and improve the shear strength, bending strength, and rotational stiffness of IMAs including slot-and-tab joints [27, 22] and through-tenon joints [28, 29, 30].

Beyond improving the integral connection characteristics, new timber plate structural forms are also continuously being proposed that introduce more favourable joint load transmission. Double-layer folded plate structures with double through-tenon joints allow direct edgewise connection between four plates at any given fold, generating a greater resistance to bending moments [31, 32]. Timber plate shell structures replace a folded geometry with a double-layer shell surface built up from integrally-attached timber boxes [33, 34]. Direct moment loading of edge joints is reduced in the structure, as moment transmission resolves as a force couple, with compressive and tensile membrane action through box face plates. Shear action occurs directly through box web plates.

A strategy to improve structural load transfer at joint locations was also recently proposed by the authors, utilising a hybrid material system [35]. Termed folded sandwich construction, the system utilises typical IMAs to first assemble a single segment, Figure 1a, and adjacent segments are then connected with a rotational press-fit (RPF) integral joint and a continuous fibre-reinforced tensile membrane, Figure 1b. Preliminary structural testing showed that with very thin 9mm plates, a semi-rigid joint action could still be achieved, with tensile action through FRP and compressive bearing through timber segments. However, precise characterisation of the RPF rotational stiffness and internal force transmission has not been investigated, nor has modelling of structural semi-rigid behaviours.

The current research study aims to comprehensively investigate the joint behaviours and overall performance of folded sandwich structures. Sections 2 and 3 first present an experimental investigation into folded arches subjected to vertical and transverse applied loading cases. Section 4 uses instrumentation data to evaluate joint rotational stiffness and develops a simplified numerical model for prediction of strength and load distribution behaviours. Section 5 develops further numerical predictions of observed core buckling and FRP fracture failure modes, followed by a discussion in Section 6 of the efficacy of the developed structural characterisation tools.

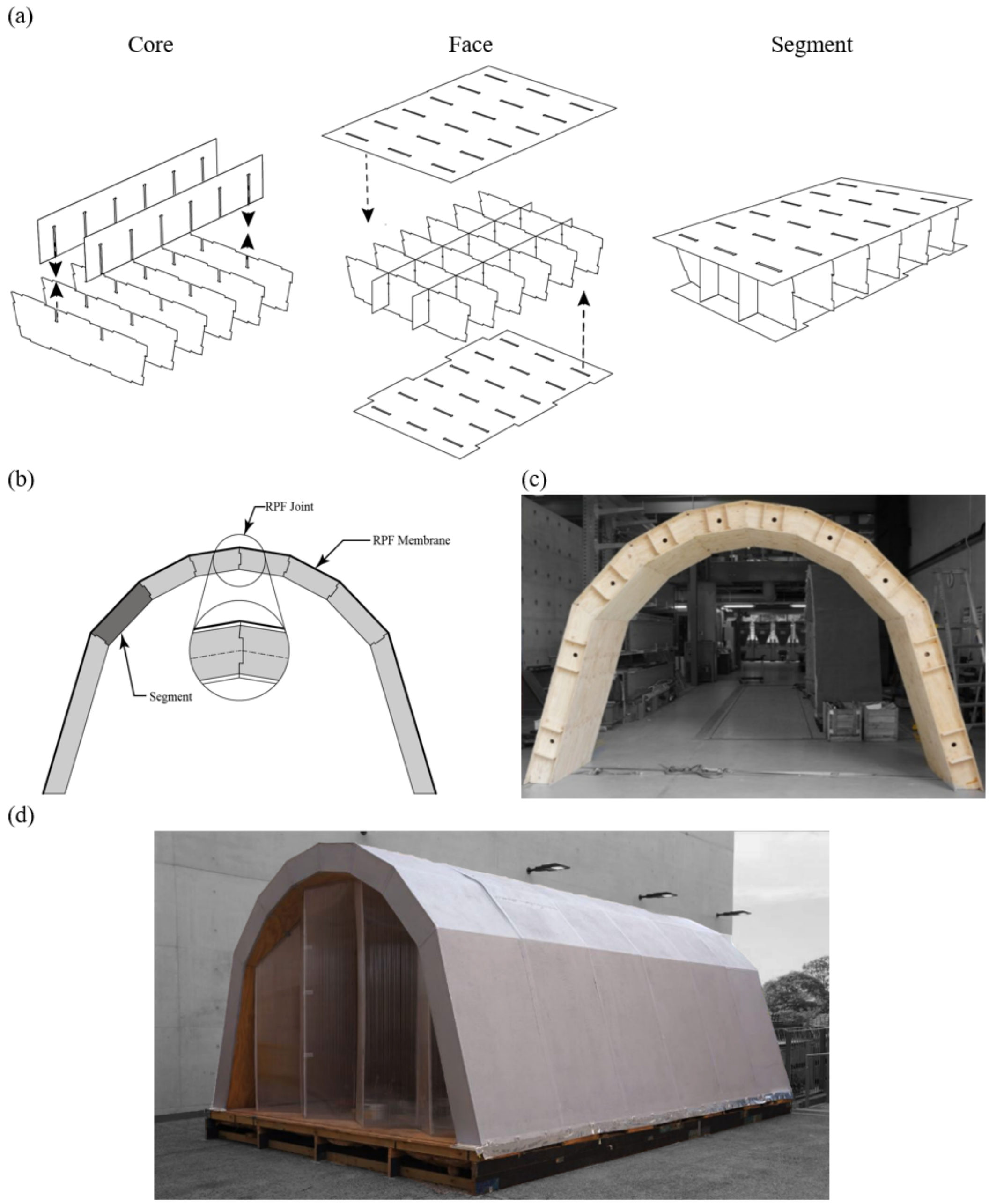

Figure 1: (a) Isometric view of exploded cores, assembled cores with top and bottom face and assembled sandwich panel segment, (b) folded state of the arch with a continuous FRP layer bonded to the top, (c) single arch structure, and (d) full house structure.

2. Experimental Testing Methodology

2.1. Hypothesised Structural Behaviour and Test Design

Consider a folded sandwich arch with an applied central point load and pinned end restraints as shown in Figure 2a. If joints are assumed to act semi-rigidly with a typical linear elastic rotational stiffness, a maximum positive (hogging) moment would be expected at the first and last joint of the arch, with a tension stress acting on outside of the joint and the compression stress on the inside. A negative (sagging) moment would be expected at the central joint, with a tension stress acting on the inside of the joint and the compression stress on the outside.

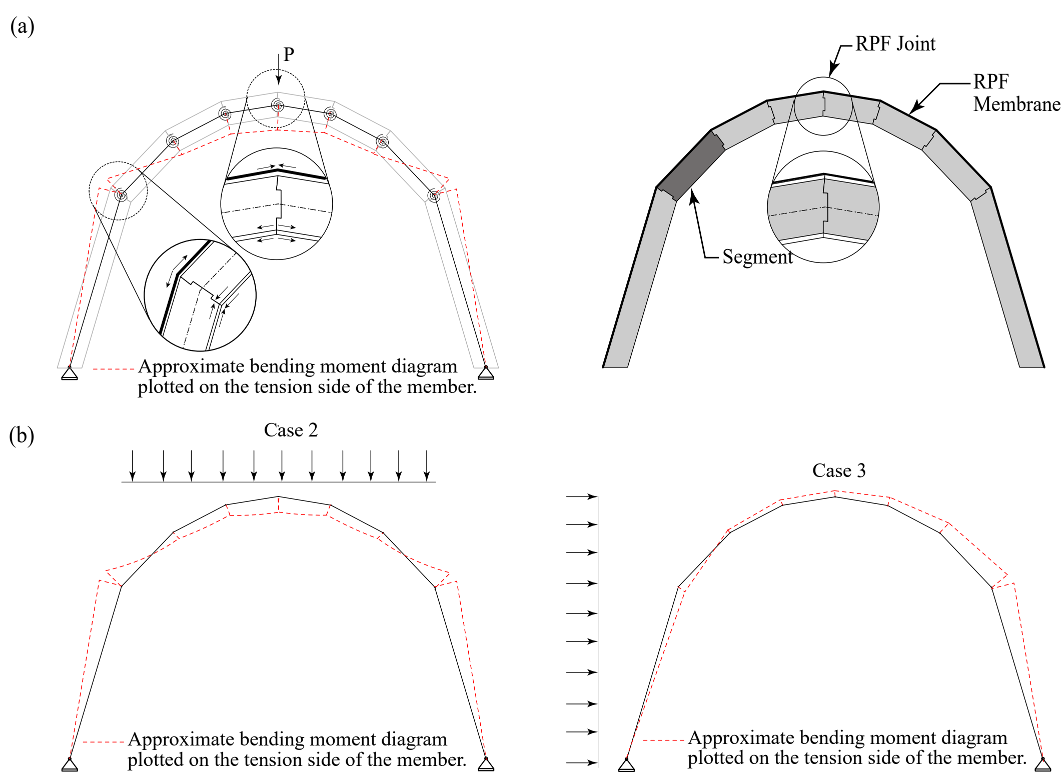

Figure 2: (a) folded arch structure with main joints force transfer mechanism and 2D simplified arch model, (b) Case 2 and Case 3 loading conditions.

However, the mechanics of joint force transfer are likely to be very different between hogging and sagging cases, due to the hybrid material construction method. In hogging cases, tension stresses can be carried through the FRP skin and compressive stresses can be carried through direct bearing between adjacent timber segments. Although the internal stress distribution is as-yet unknown, most of the section is utilised and one would expect the joint to act with a reasonably high rotational stiffness.

In sagging, there is no load transfer mechanism except for bending of the FRP skin itself and some minimal friction between timber segments. Joint rotational stiffness would therefore be expected to be near zero. For the structure to carry load, joints acting under sagging moments must develop into hinges and distribute forces to adjacent joints acting under hogging moments. In the case of the system shown in Figure 2a, a statically determinant three-hinged arch structure will arise if the central joint develops into a hinge, but preservation of stability beyond this point requires adjacent segments to provide sufficient rigidity to prevent sagging action developing in any other joints.

Assuming global stability can be preserved through such geometric stiffening, the strength of the system is predicted to be governed by the strength of joints under hogging action. Potential failures could be (1) tensile tearing of the FRP layer; (2) compressive rupture in the timber segment; or (3) some local stability failure in the segment itself, for example local buckling in longitudinal plates or pop-off of integrally-attached inside face plates [36, 37].

To investigate the interaction between applied loadings, internal force distribution, joint behaviours, and overall structure behaviours, a program of experimental testing was undertaken to induce different sagging and hogging conditions at internal joints in a folded sandwich arch. Load Case 1 is as described above, with a single central vertical load to induce a hinge development in the central hinge. Case 2 and 3 are distributed vertical and horizontal loading conditions as shown in Figure 2b. Case 2 is designed to reduce hogging moments in central arch joints and so force a greater load redistribution to outer joints. Case 3 is designed to induce a sagging moment in the first (left-hand side) arch joint.

2.2. Specimen Manufacture

Folded sandwich arch specimens were constructed with overall dimensions of 4.5 m (L) x 1.18 m (W) x 3.0 m (H). Arches are comprised of eight individual sandwich segments, with each segment composed of six longitudinal core plates, two cross core plates, and top and bottom face plates. Longitudinal and cross core plates were connected with integral notch joints and longitudinal core and face plates were connected with integral tenon joints, as shown in Figure 1a. Plate material was 9mm thick F8/F11 grade structural plywood (manufacturer Carter Holt Harvey, grade system from Australian Standard AS1720 Timber Structures), composed of three 3mm plies and ply orientation of 0°/90°/0°. All timber parts were cut on a CNC router, with integral connections calibrated to give a tight friction-only fit. An extended description of the integral connection parameters and digital fabrication workflows is available in [35]. Detailed arch segment parameters are also provided in Supplementary Material S1.

The assembled segments were arranged on a flat surface and bonded to a continuous fibre reinforced polymer (FRP) skin on the exterior top skin using chemical adhesion. The FRP material was a Biotex Flax fibre, 400g/m2 2x2 twill weave, with a Gurit AMPREG 22 epoxy matrix. A fast 3-hour hardener was used on segments and a slow 24-hour hardener was used at joints, with the differential cure time used to fold the arch into its final shape, from flat, after approximately 6 hours [38]. Two specimens were manufactured for each case, with a typical specimen shown in Figure 1c and all six specimens shown in Figure 1d. The Case 2 Arch 1 specimen suffered some damage during erection, with an FRP fracture along one joint; the arch was repaired for testing with additional FRP.

2.3. Testing Apparatus and Instrumentation

The testing apparatus for all three load cases is shown in Figure 3. Load application was from Enerpac double-acting actuators, manually controlled by a single pressure pump. Actuators were model RR1012, with a 100 kN maximum load capacity and a 300mm maximum displacement capacity. Actuators were connected to the structure with a steel beam assembly, comprising a top and bottom pair of steel sections, rigidly clamped to segments by high-strength threaded bolts. A 2.5 ton ratchet strap was used to connect actuators to the middle of bottom steel beam for Cases 1 and 2, and the middle of the top steel beam for Case 3. Arches were fixed against horizontal movement at the base and for Case 3 arches were additionally prevented from uplift using hold-down ratchet straps. Actuators were anchored directly to a strong floor for Cases 1 and 2, and a steel reaction frame for Case 3. Applied force was measured with in-line load cells attached at each actuator. Global displacement was measured with two linear variable displacement transducers (LVDTs) attached to both sides of the middle joint of the arch for Case 1 and 2, and on joint 7 for Case 3 as is shown in Figure 4.

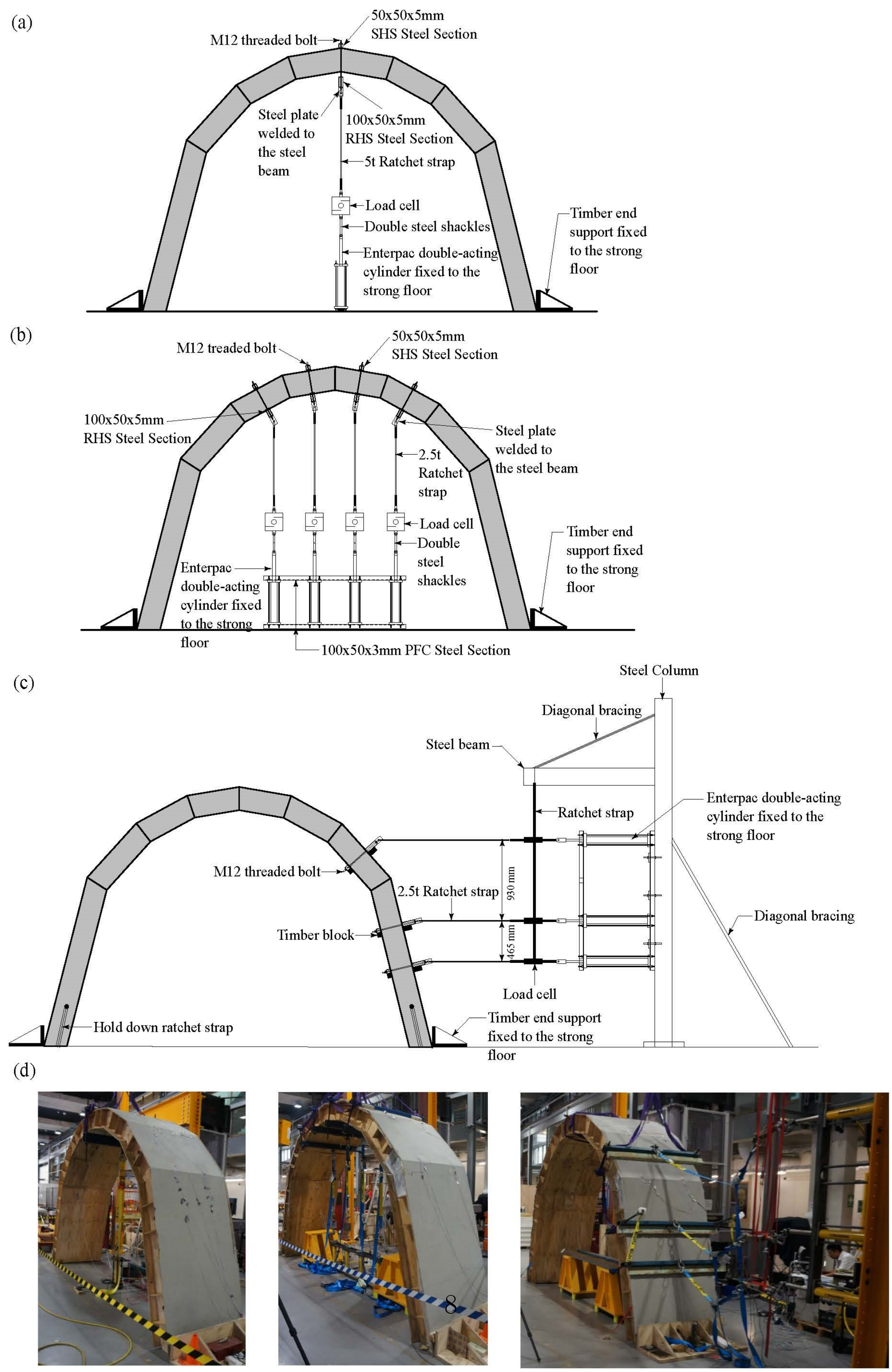

Figure 3: Arch testing configurations with schematic view for (a) Case 1, (c) Case 2, and (e) Case 3. (d) 3D view for Cases 1 to 3.

Measurement of internal force transfer at folded joints is of key interest in evaluating the stiffness and strength characteristics of the folded sandwich structural system. Digital Image Correlation (DIC) was used to measure the strain distribution on the outer FRP layer for Case 1 tested specimens and on core plates for Case 2 and 3 tested specimens. Core strain was collected at first or last joints, as these joints were judged likely have maximum hogging moment loads. Measured surface faces were first painted white, with subsequent application of a speckle patterns with a 0.5mm speckle size. Speckle size was selected based on the joint field view size which is approximately 250mm high by 100mm wide. Image capture was conducted with VIC-3D software at two second increments.

As available DIC equipment was only sufficient to measure one surface per specimen, strain gauge instrumentation was attached to each joint. Strain gauge data also allows for system load transfer behaviours to be assessed, and for material strain and failure strength to be assessed. 42 gauges were used for each specimen as shown in Figure 4, with gauges attached to each side of each joint, along two rows on the top FRP surface and one row for the bottom surface. Strain gauges are of type BA120-10AA grade A with a resistance of 120.4±0.1 Ohms and gauge factor of 2.21±1%.

3. Experimental Results

3.1. Force-displacement curves and failure modes.

Force-displacement curves obtained from the three cases are shown in Figure 5, with key values summarised in Table 1. For Case 1, Arch 1 and 2 had similar peak forces of 24.4kN and 23.6kN, respectively, however they exhibited different failure modes: Arch 1 had failure from tear-out of the FRP layer at joint 1 whereas Arch 2 had failure from plywood compressive rupture at joint 7, as shown in Figure 6a-b. For Case 2, Arch 1 had a maximum total force of 21.8kN, again with failure through tear-out of the FRP layer at joint 1. For Arch 2, the peak force was higher by 44% at 31.8kN and failure was plywood compressive rupture at joint 1 as shown in Figure 6c. The displacement was not recorded for Arch 1 due to unknown error in the displacement instrument. Opening was observed in the central joint opening for all Case 1 and Case 2 arches as shown in Figure 6e. For Case 3, peak force in Arch 1 was 11.1kN and 15% higher in Arch 2 at 13.0kN. Both arches exhibited failure through tear-out of the FRP layer at joint 7 and showed opening at joint 1, as shown in Figure 6d-e.

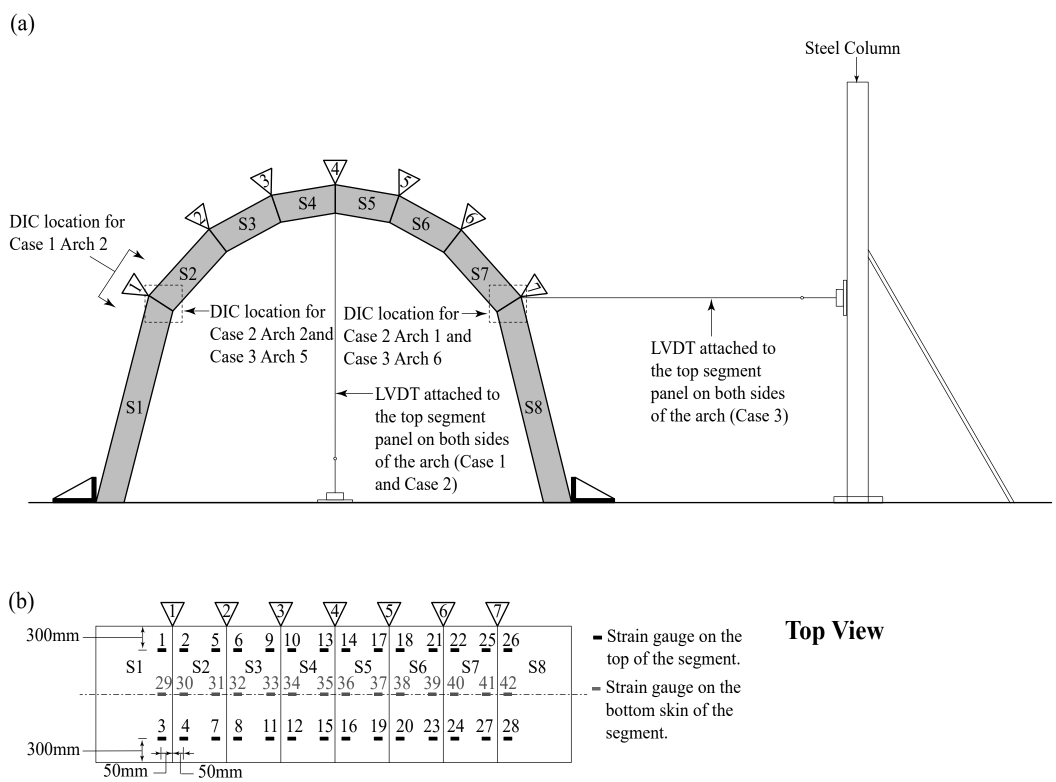

Figure 4: Arch testing instrumentation setup (a) front view and (b) top view with strain gauge distribution.

For all Cases and arches, failure occurred at the joints where maximum hogging moment would be expected, opening occurred at the joint where a maximum sagging moment would be expected, and arches were able to carry substantial load despite joint opening. This agrees with the hypothesised structural behaviour: joints acting under sagging moments develop into hinges and distribute forces to adjacent joints acting under hogging moments.

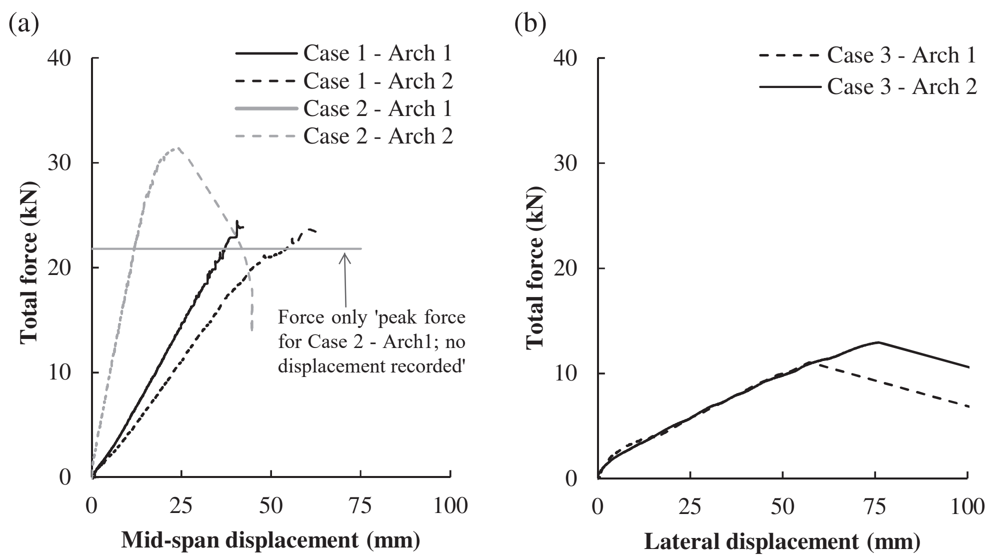

Figure 5: Force-displacement curve for (a) Case 1 and Case 2 and (b) Case 3.

Table 1: Summary of results from arch experimental testing.

Case	Arch No.	Total Force (kN)	Maximum displacement (mm)	Failure mode
1	1	24.4	42.7	FRP fracture
	2	23.6	60.6	Plywood rupture
2	1	21.8	-	FRP fracture
	2	31.5	45	Plywood rupture
3	1	11.05	57.3	FRP fracture
	2	12.95	76	FRP fracture

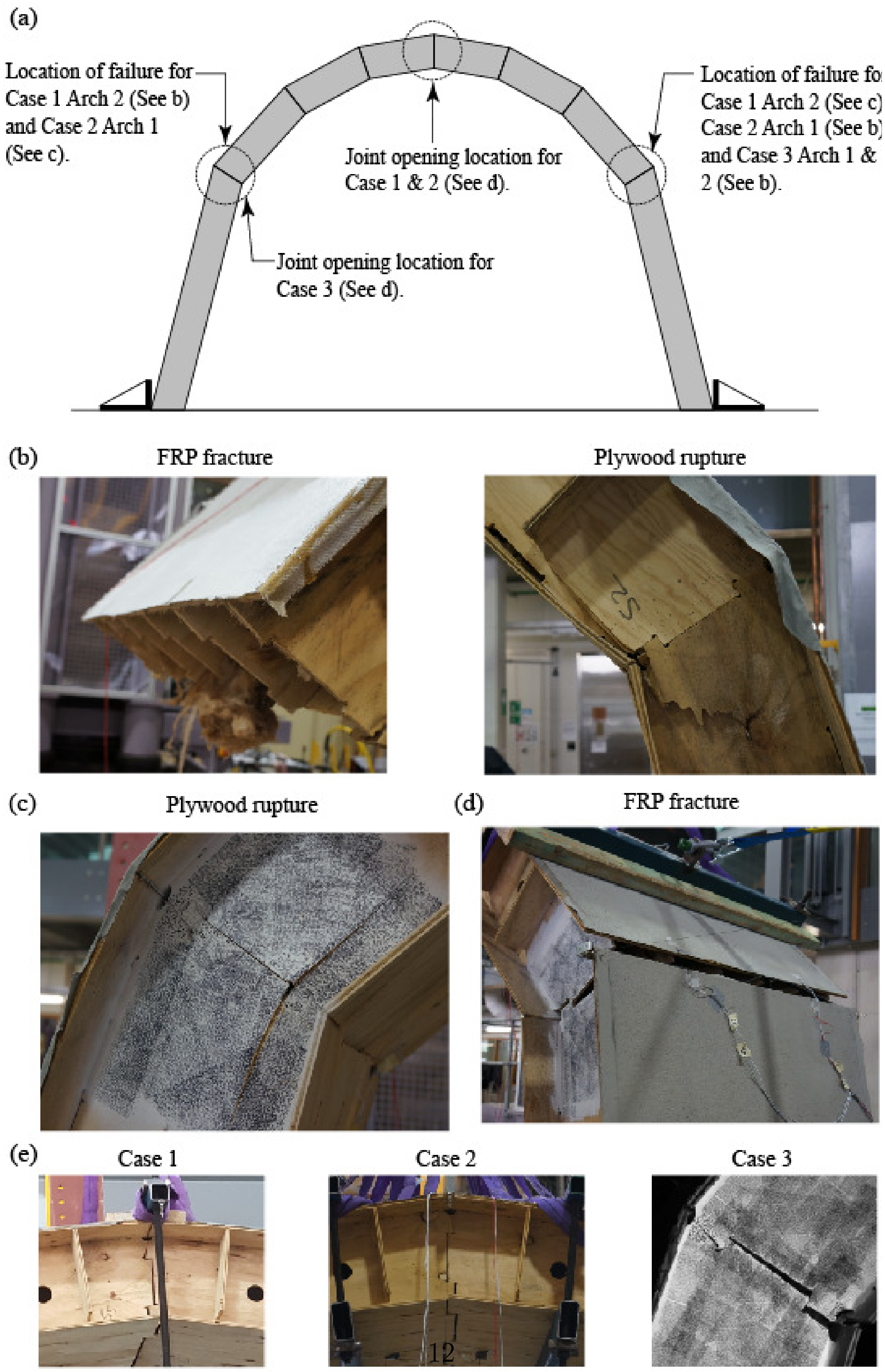

Figure 6: (a) Failures and joint opening locations, (b) failure mode for Case 2, (c) failure mode for Case 2, (d) failure mode for Case 3, and (e) joint opening for all cases.

3.2. Strain gauge results

The load distribution and force transfer mechanism behaviour can be more closely investigated using data from strain gauge instrumentation installed along the top and bottom skins of the folded arches. Figure 7 shows the strain values for Case 1 Arch 2, recorded at different loading values. A comparison between strain gauges 1, 2, 3 and 4 at joint 1 and top skin DIC data is shown in Figure 8a-b and demonstrates good correspondence, confirming the validity of the collected strain gauge data.

Several observations can be made as to load distribution. First, with respect to load distribution through the section, it can be seen that strain in the bottom skin is almost zero in all locations. There is a very slight strain recorded near end joints however this is small as compared with top skin tensile strains. It can be concluded that the bottom skin has little compressive force transmission, which instead must occur through core plate load transmission. This will be investigated further in the next section.

Second, with respect to load distribution across the arch width, strain distribution between left and right sides on the top skin are similar, indicating a symmetric load distribution. This is supported by the top surface DIC strain field measurements collected for Case 1 and shown in Figure 8b; stress is approximately symmetric across the arch but with stress concentrations at core locations.

Third, with respect to load distribution along the arch, peak tensile strains in the top skin are recorded in end joints, corresponding to expected regions of the maximum hogging loads. However, a peak strain is also seen near the opening central joint. This may be related to some localised strain in the FRP from hinge formation; or it may be related to some sensitivity in strain gauge location near regions of joint stress concentration. Strain increases near opening joints were not observed in other Cases.

Figure 9a-c shows strain value collected for Case 2 Arch 2 and Figure 9d-f shows strain value collected for Case 3 Arch 2. Bottom skins are again seen to carry almost no load, noting the change in y-axis scale for bottom skin plots. Top-skin strains are again symmetric across the width as evidenced by similarity between front and back-side strains. Of key importance though is the clear load distribution behaviour shift between vertical and transverse loading cases. For Case 2, maximum top-skin tensile strains and hogging moments occurred in end joint failure locations; minimum top-skin strains (near zero) occurred in the central joint hinge location. For Case 3, maximum

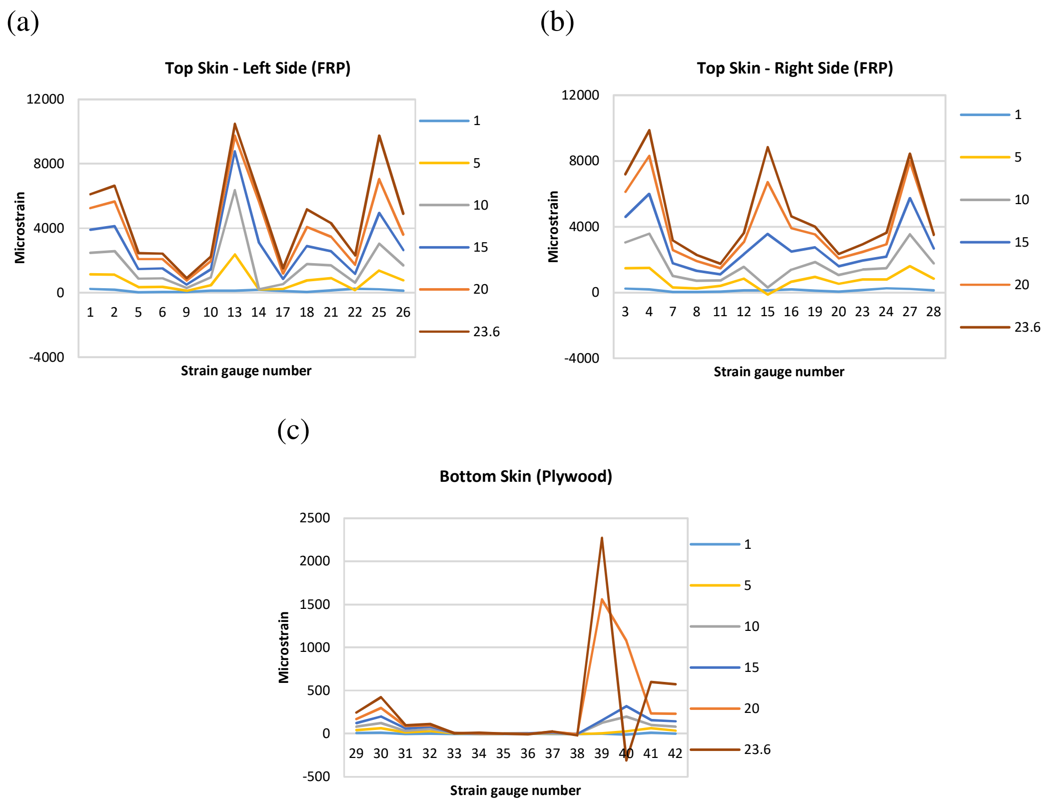

Note: Positive value of strain indicates that the strain gauge elongates (in tension). However, a negative value indicates that the strain gauge is shorten (in compression).

Figure 7: Strain distribution along Case 1 Arch 2 perimeter on (a) top skin left side, (b) top skin right side, and (c) bottom skin.

strain occurred at joint 7 at the observed failure and minimum strain occurred at joint 1 at the observed hinge location.

There were some inconsistencies in measured strain between specimens for Case 1 and 2, due to errors in specimen manufacture and testing. For Case 1 Arch 1, a loss of wire connectivity occurred during testing due to improper soldering; collected data for this specimen is therefore not considered. For Case 2 Arch 1, this arch was repaired at the fabrication stage and imperfections were seen to give rise to inconsistencies in collected strain data; collected data for this specimen is therefore also not considered. Case 3 Arch 1 data has very similar strain values recorded to Arch 2.

3.3. Digital Image Correlation results

For Case 2 and 3, DIC instrumentation was used to monitor core behaviour in joint regions with predicted maximum hogging and sagging moment. This section first describes the collected strain data and Section 4.3 will later describe its use in developing a joint moment-curvature relationship for use in numerical analysis of folded sandwich structures.

For Case 2, the first joint for Arch 2 and last joint for Arch 1 were monitored with DIC instrumentation. The strain values at 5kN loading showed a maximum compression strain occurred at the innermost end of the core, with 4550 microstrain for Arch 1 and 3786 microstrain for Arch 2 as shown in Figure 10a-b, which can be considered a reasonably symmetric load distribution. The strain distribution indicates that the bottom part of the joint

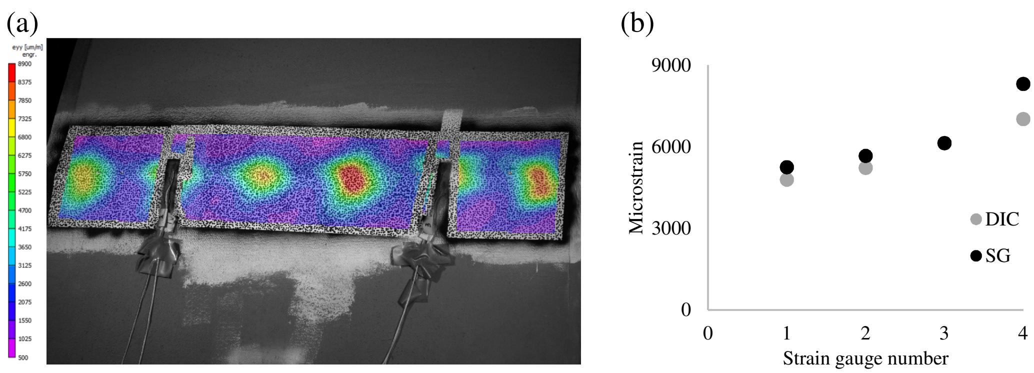

Figure 8: Strain distribution on the top skin of the first joint of Case 1 Arch 1; (a) using DIC data and (b) using strain gauge data.

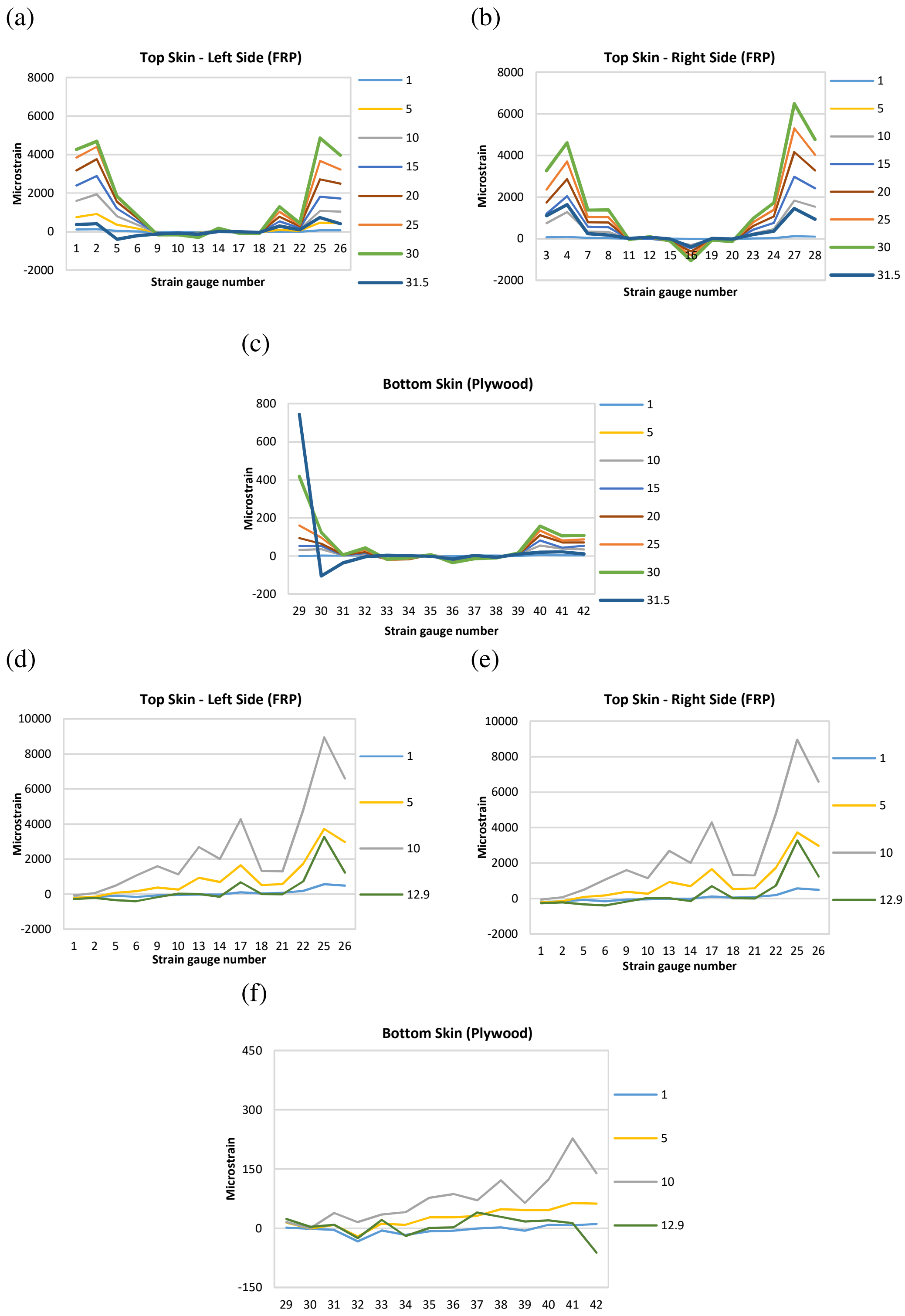

Note: Positive value of strain indicates that the strain gauge elongates (in tension). However, a negative value indicates that the strain gauge is shorten (in compression).

Figure 9: Strain distribution along (a-c) Case 2 Arch 2 perimeter on (a) top skin left side, (b) top skin right side, and (c) bottom skin; and (d-f) Case 3 Arch 2 perimeter on (d) top skin left side, (e) top skin right side, and (f) bottom skin.

is subject to compression stresses, transferred through bearing over a compression zone with depth c. The top part of the joint opens up (indicated as tensile strain) and so tension stresses are transferred through the FRP layer. A schematic of the strain distribution over the joint is shown in Figure 10c.

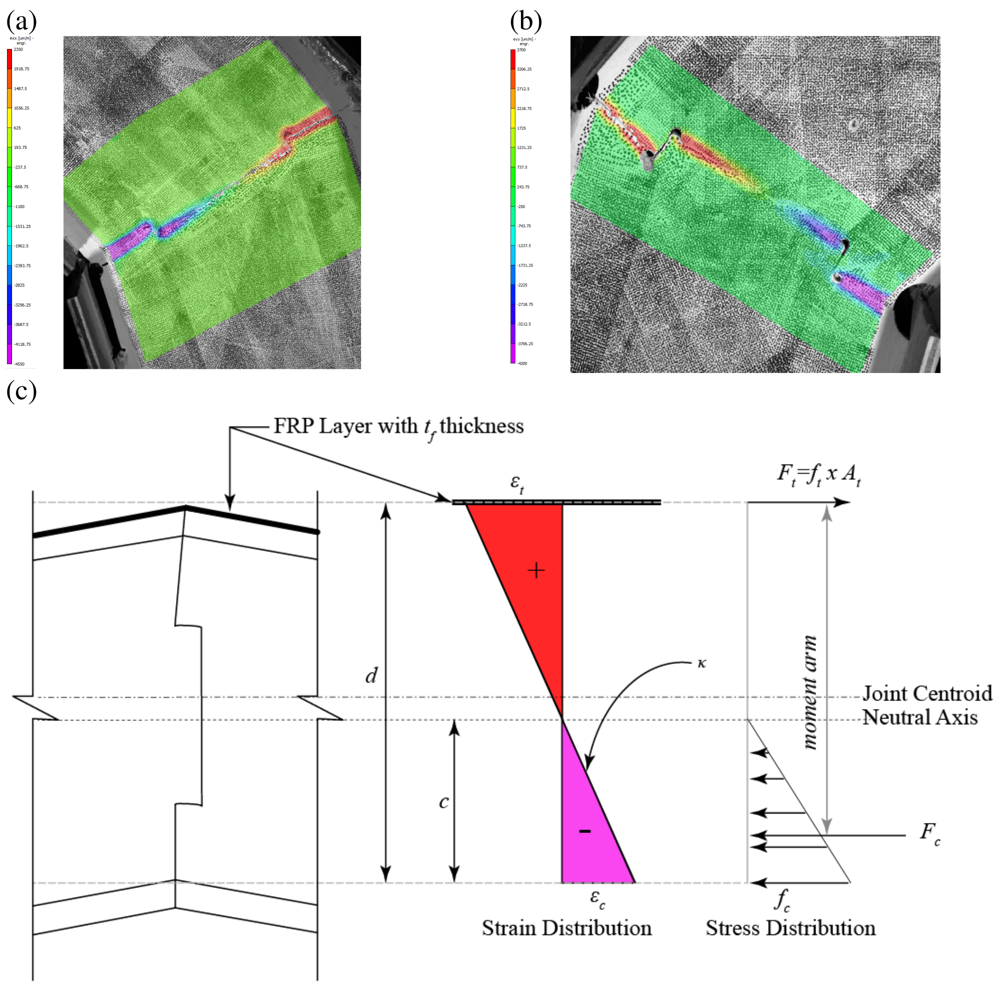

Figure 10: DIC analysis data for Case 2 (a) for Arch 1, (b) for Arch 2, and (c) schematic sketch of strain and stress distribution over the joint.

For Case 3, the first joint for Arch 1 and last joint for Arch 2 were monitored with DIC instrumentation, shown in Figure 11a-b. Joint 1 in Arch 1 is under negative moment, with tension on the bottom part of the joint.

Thus, joint opening is observed with minimal or no resistance to opening. Joint 7 in Arch 2 is under positive moment in which the bottom part of the core was under compression and the top skin was under tension as shown in Figure 11b, with joint strain and stress distribution similar to that for Case 2 joints.

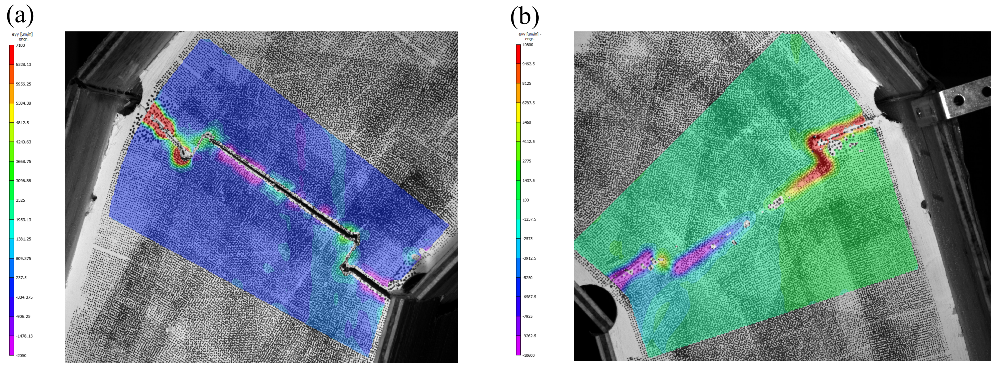

Figure 11: DIC analysis data for case (3) (a) for Arch 1 and (b) for Arch 2.

3.4. Results summary

Experimental testing of the arches under three different load cases has shown two failure modes: FRP layer tear out and buckling of longitudinal core. Both failure modes occurred at the first/last joint in the location of maximum hogging moment. Joint opening has been observed in all tested arches in locations of sagging moment, but the structural system maintained stability and strength through load redistribution to adjacent joints acting under hogging action.

DIC data showed joint force transmission occurs primarily through compressive bearing the core plate and tensile stress through the FRP skin, corresponding to the two observed failure modes. Strain gauge data has shown minimal compressive forces were transferred through the bottom skin and as such, there were no local stability failure in segments from use of integral joints. However, the bottom skin is thought to affect the lateral buckling of the longitudinal core plates, which will be investigated further in Section 5.1.

4. Numerical model for structural response prediction

4.1. Method

A simplified numerical model is proposed for the evaluation of the structural behaviour of folded sandwich arch structures. With reference to Figure 12, an arch model is implemented with 2D frame elements, with a composite cross section composed of the longitudinal plywood cores and a top FRP skin. Elements are connected with discrete hinges, with a defined nonlinear moment-curvature relationship obtained from joint strain data. The model was implemented in SAP2000 structural analysis software, which has a 'plastic' hinge method that allows for input of nonlinear hinge attributes. Hinge length was calculated as per the equation provided in Supplementary Material S3 and found to be 0.1 of element length for this method. The method of plastic hinge calculation was proposed in [39, 40].

A displacement-controlled nonlinear static analysis was used to allow for evaluation of elastic and inelastic hinge behaviour. Applied analysis loads matched the loading patterns of the three experimental test cases. For Case 1 and Case 2, target displacement was assigned as 80mm for the middle joint in the downward direction (-y-axis). For Case 3, target displacement was assigned as 80mm for joint 7 in the lateral direction (+x-axis). The boundary condition for all cases was pinned restraint at base nodes. The selection of 80mm target displacement was based on the ultimate displacement from the experimental testing.

4.2. Material model

Linear material properties were used for the model. Plywood material properties were calculated based on available hoop pine veneer testing data, a timber species typically used to manufacture plywood sheets in Australia [41]. The 9mm plywood plate is composed of three layers of pine veneers, each 3mm thick. The outer layers have veneers with grain directions parallel to the plywood sheet with a modulus of elasticity of 13,000MPa and compressive strength of 31MPa. The middle layer has veneer perpendicular to the plywood sheet with a modulus of elasticity along the plywood sheet length of 636MPa and compressive strength of 10MPa. Hence, the uniaxial composite beam modulus of elasticity for the section was found as 8879MPa which is the sum of two-third of modulus of elasticity for the outer layers and one-third of modulus of elasticity for the middle layer. Similarly, the uniaxial compressive strength was found as 24MPa.

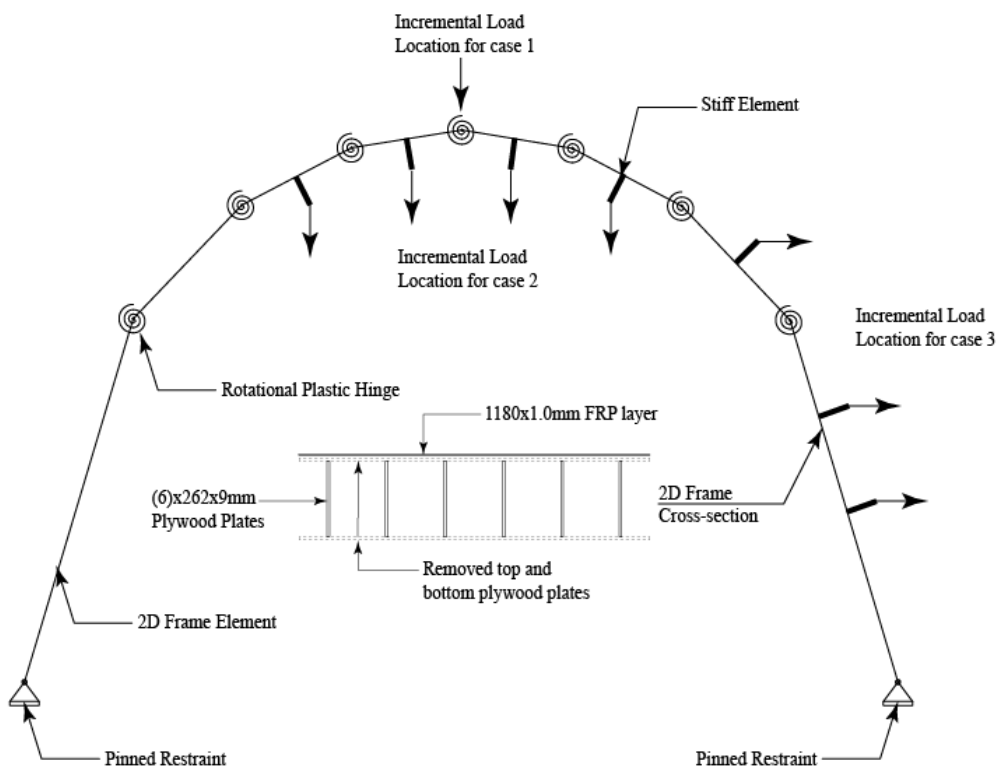

Figure 12: 2D frame model using SAP2000.

FRP material properties of the Biotex Flax 400g/m^2 layer were experimentally obtained according to ASTM D3500. Ten samples were tested under uniaxial tensile testing to obtain the average tensile strength and uniaxial modulus of elasticity of the FRP layer. The average axial tension strength and the modulus of elasticity were found to be 39.8MPa and 3709MPa, respectively. Further details are provided in Supplementary Material S2.

4.3. Moment-curvature data extraction and relationship

4.3.1. Strain data

The moment-curvature ($M - \kappa$) relationship is dependent on the slope of the line that connects the maximum compression and tension strain across the cross-section of a beam subjected to bending and axial force [39]. The maximum tensile strain can be obtained for all tested arches from strain gauge instrumentation, however the maximum compressive strain can only be obtained for Case 2 and Case 3, where DIC instrumentation was used in the joint region. The $M - \kappa$ relationship is therefore only developed for these two cases.

For Case 2 Arch 2, strain data was sampled at 5, 10, 20, 25, 27, and 31.5 kN (ultimate) load. Joint 1 strain gauge data, SG1-1 and SG-3, were averaged to obtain maximum tensile strain ε_t. The maximum compressive strain ε_c was obtained from DIC data at the same load increments, at the bottom of the core plates where maximum bearing stress occurred, as described in Section 3.3. For Case 3 Arch 2, strain data was sampled at 5, 9, 10, and 12.95 kN (ultimate) load, with DIC and strain gauge data from joint 7 (SG-26 and SG-28). Obtained values are summarised in Table 2 and plotted in Figure 13a and c.

4.3.2. Development of moment-curvature relationship of the RPF joint.

Curvature κ is calculated based on the slope of the resulting strain line between maximum compressive and tensile strains [39], as shown in Figure 10c and as per the following equation:

$$\kappa = \frac{\varepsilon_c + \varepsilon_t}{d} \tag{1}$$

where d is the total section depth and equal to 276mm. The beam bending section capacity can be calculated as per the following equation [39]:

$$M = (f_t \text{ or } f_c) \times (A_t \text{ or } A_c) \times \text{moment arm} \tag{2}$$

Table 2: Summary of extracted strain gauge data for specified load values for (a) Case 2 Arch 2 and (b) Case 3 Arch 2.

(a)

	Strain (Microstrain)					
Loading value (kN)	5	10	20	25	27	max. Loading
Average tensile strain in FRP ε_t	1085	2334	4911	6197	6702	7897
Compressive strain in plywood ε_c	3786	7236	17339	19816	23365	39982

(b)

	Strain (Microstrain)			
Loading value (kN)	5	9	10	max. Loading
Average tensile strain in FRP ε_t	2776	5850	7297	8358
Compressive strain in plywood ε_c	20664	40380	46079	57700

where f_t is the tension stress of the FRP can be found by multiplying the tension strain (ε_t) by the modulus of elasticity of the FRP layer (E_t). A_t is the tension area of the FRP (layer thickness t_f times arch width b) and A_c is the compression area of the plywood (compression zone depth c times b). c was found from DIC compression strain zone joint data and also used to calculated the moment arm as the the distance between the compression and tension resulting forces, as shown in Figure 10c. Hence, by substituting f_t, A_t, and the moment arm into Equation 2, the moment M at a specific loading point can found as:

$$M = (\varepsilon_t \times E_t) \times (t_f \times b) \times (d - \frac{c}{3} - \frac{t_f}{2}) \quad (3)$$

The calculated moment-curvature values are summarised in Table 3 and plotted in Figure 13b and d. The $M - \kappa$ curve obtained from experiments can be seen to be approximately bilinear, so a bilinear hinge description was implemented in the numerical model. Bilinear parameters are thus the three points of Case 2 and Case 3 curves, connected by the shown dashed line. There can be seen to be a difference between Case 2 and Case 3 $M - \kappa$ curves, with a larger curvature seen in Case 3 when at a similar moment loading to Case 2. This may be due to the base support condition, which is not perfectly pinned and may behave differently under vertical and lateral loading conditions, for example allowing some additional horizontal movement or uplift at inside edges.

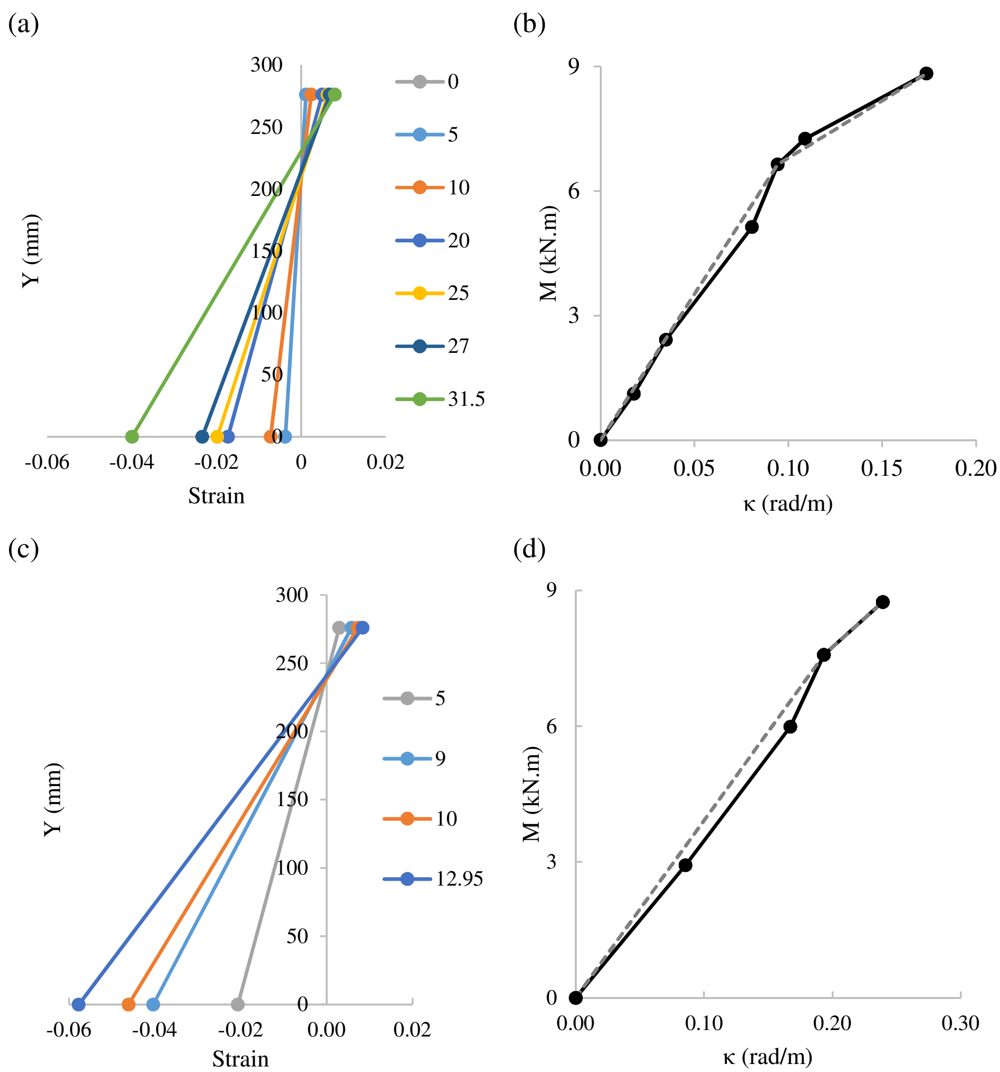

Figure 13: For Case 2: (a) strain distribution along the section, (b) Moment-curvature relationship curve. For Case 3: (c) Strain distribution along the section, (d) Moment-curvature relationship curve.

Table 3: Summary data for moment-curvature relationship evaluation, for (a) Case 2 and (b) Case 3.

(a)

Loading Stage (kN)	0	5	10	20	25	27	31.5
Stress in the FRP f_t (MPa)	0	4	8.7	18.2	23	24.9	33.4
c (mm)	0	125.2	117	110.8	92	84.2	60.3
M (KN.m)	0	1.1	2.4	5.1	6.6	7.3	8.8
κ (rad/m)	0	0.018	0.035	0.081	0.094	0.109	0.173

(b)

Loading Stage (kN)	0	5	9	10	12.95
Stress in the FRP f_t (MPa)	0	10.8	21.5	27.8	31
c (mm)	0	138.3	118.3	114.4	109.1
M (kN.m)	0	2.9	6	7.8	8.7
κ (rad/m)	0	0.085	0.167	0.194	0.239

4.4. Implementation and Results

4.4.1. Prediction of peak force and stiffness

The numerical analysis for all cases was first implemented with the bilinear hinge description obtained from Case 2, with results plotted in Figure 14. As a displacement-controlled analysis method was used, the force response is taken as the sum of the support vertical reaction forces for Case 1 and 2, and sum of horizontal reaction forces for Case 3. Displacement is taken as vertical displacement in the central joint for Case 1 and 2, and horizontal displacement of joint 7 for Case 3.

A good estimation for peak force is obtained for both Case 1 and 2. For Case 1, the numerical prediction of 22.7kN is 7% and 4% less than the maximum experimental force for Arch 1 and Arch 2, respectively. For Case 2, the numerical prediction of 31.3kN is 0.6% less than Arch 2 but 44% greater than Arch 1, noting that Arch 1 was the damaged specimen which was repaired prior to testing.

For Case 3, the numerical prediction obtained using the Case 2 hinge description did not give a good prediction of peak force; the 8.5kN predicted maximum force is 23% and 35% lower than Arch 1 and Arch 2, respectively. However, numerical simulation using the Case 3 hinge description gave a significantly better prediction; the 10.2kN predicted maximum force is 8% and 21% lower than Arch 1 and 2, respectively.

With respect to prediction of the stiffness of folded arch structures, the numerical models gave varied results depending on the case. Case 2 and Case 3 models both gave good prediction of experimental stiffness values when using their respective hinge models. The Case 2 hinge model was applied to Case 1 and the resulting curve showed higher stiffness than seen experimentally. Further study is needed to determine whether the decreased stiffness in Case 1 is due to a change in joint behaviour or due to a weakened load distribution behaviour arising from the concentrated loading arrangement.

It can be concluded that the simplified model gives reasonable estimation of strength, but is highly dependent on the hinge $M - \kappa$ characterisation. The capacity for simplified models to predict stiffness is inconclusive from the available experimental data, but from preliminary assessment it is feasible in some cases. Certain model simplifications, in particular linear material properties, could likely be revised to improve response prediction in the elastic-plastic transition phase.

4.4.2. Prediction of load distribution

The tensile skin strain data, used to establish load distribution behaviour in experimental specimens, provides a second way to verify the efficacy of the simplified numerical modelling approach. Bending moments M and axial forces P from elements in the simplified numerical model can be converted to stress at the tensile surface using [42]:

$$\sigma_t = \frac{M y_{cg}}{I_{cg}} \pm \frac{P}{A} \tag{4}$$

where y_{cg} is the distance between the section centre of gravity to the tensioned FRP layer, I_{cg} is the second moment of area around the centre of gravity axis, and A is the cross-sectional area. P is positive for tension and negative for compression.

Section properties are calculated using the transformed section method, converting plywood material regions to equivalent FRP section using modular factor, n, calculated as [42]:

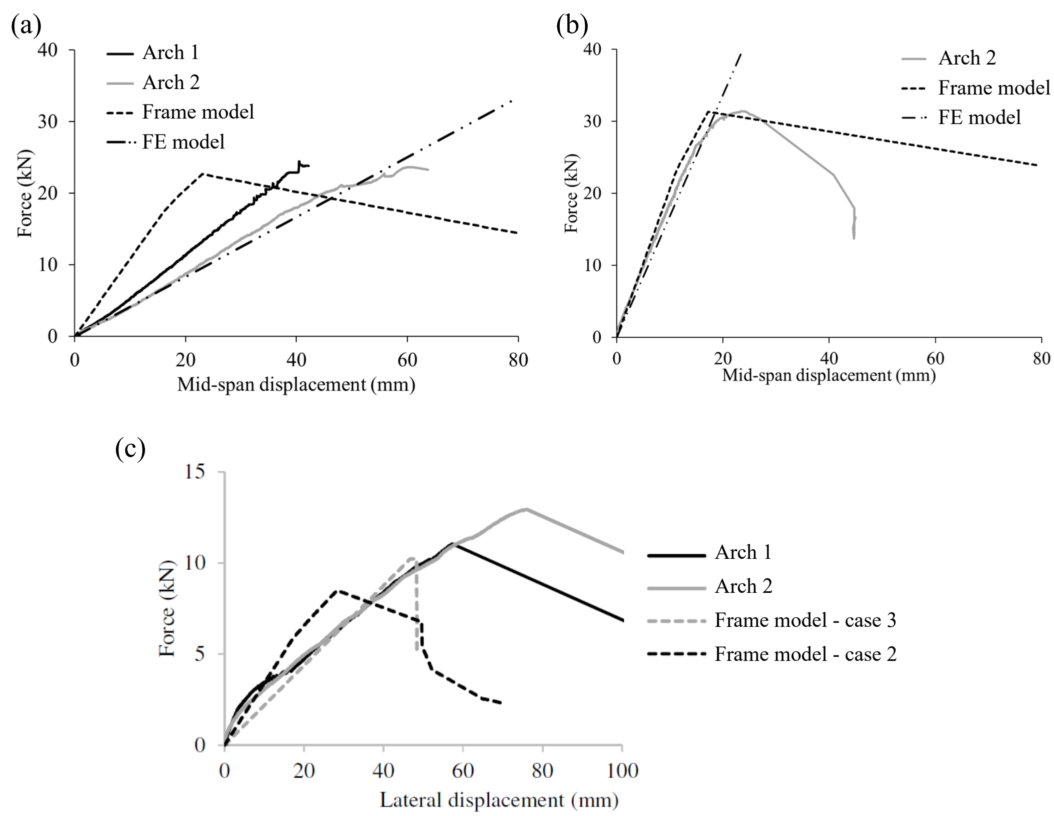

Figure 14: Force-displacement curve for (a) Case 1, (b) Case 2 and (c) Case 3.

$$n = \frac{E_t}{E_f} \tag{5}$$

where E_t and E_c are the modulus of elasticity of FRP and plywood, respectively. Once the stress applied on the FRP layer is found, the strain, ε_t, can be calculated as:

$$\varepsilon_t = \frac{\sigma_t}{E_p} \tag{6}$$

Based on the above, numerical strain values were calculated to the left and right of each joint, corresponding to the strain gauge instrumentation locations. For Case 1, experimental and extracted numerical strain data is plotted at 10kN and 20kN applied load in Figure 15a-b. Case 2 is plotted at the same loading stages in Figure 15c-d and Case 3 is plotted at 5kN and 8kN applied load in Figure 15e-f. In general, it can be seen that the numerical model has a good prediction of the load distribution behaviour obtained from strain gauge data. For example, for Case 2 and 3, the predicted maximum strain value and joint location corresponds to measured values. However, for Case 1, strain values recorded by strain gauges are very high at central joint. This high strain value may be related to the joint opening or stress concentration near the load application point. A similar distortion in strain distribution in strain gauges can also be seen adjacent to loading points in Case 2 for SG-5-6 and 21-22, and Case 3 for SG 17-22. The loading method introduced in the experimental testing may therefore introduce additional loading which is not presented in the numerical model.

5. Numerical models for prediction of failure modes

5.1. Local buckling of plywood at the joint location

The core buckling behaviour was hypothesised to be due to misalignment of segments during the structure assembly process, causing a transverse offset between core plates acting in bearing. To estimate the impact of this on system strength, a finite element linear buckling analysis was conducted on a single arch core geometry. Analyses were conducted on a perfect core geometry and also on geometries with an artificial defect introduced in the form of an eccentricity between core plates at joint 7. The eccentricity was introduced in 1mm increments from 0 to 6mm (0mm corresponding to a perfect geometry).

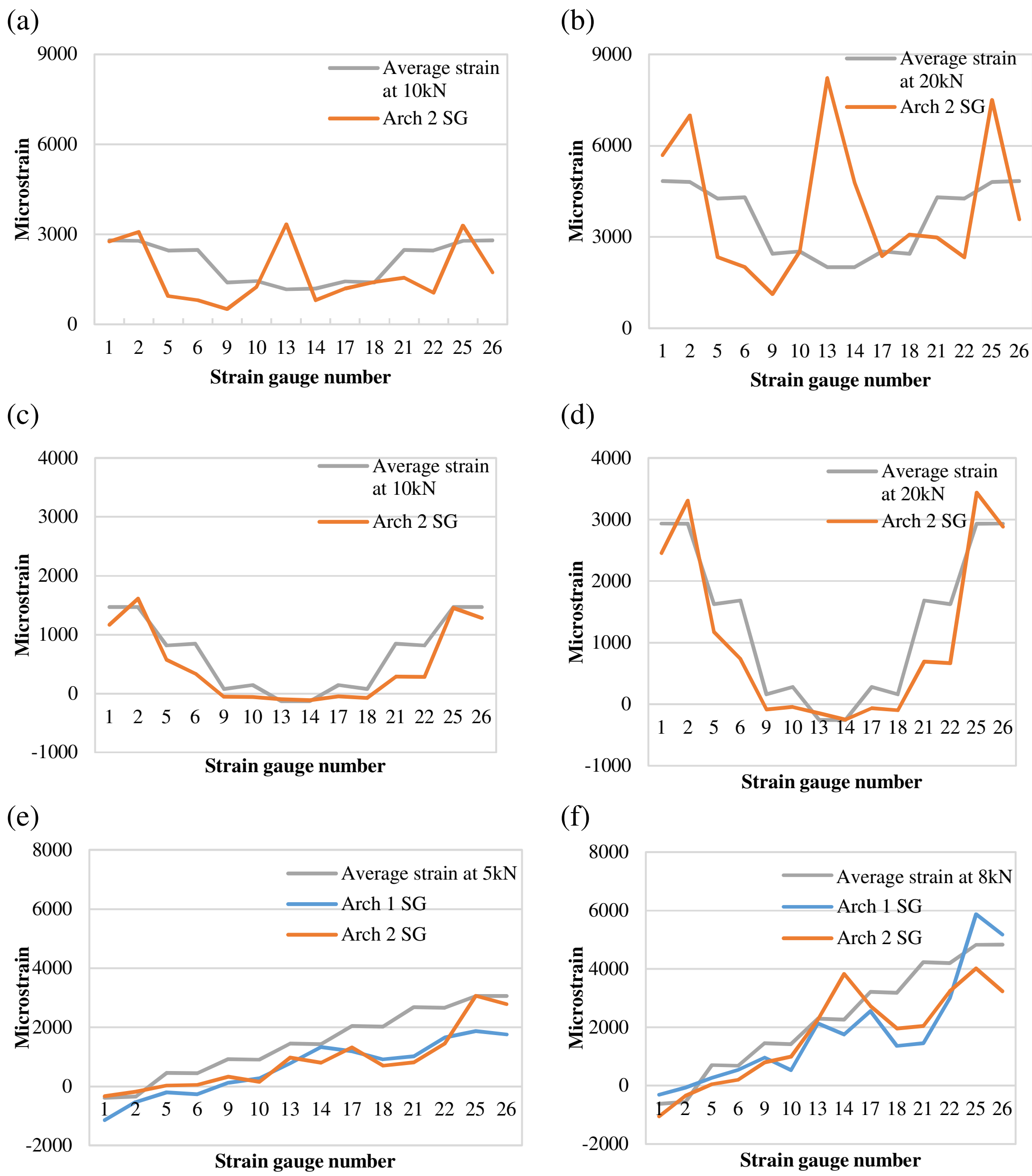

Figure 15: Comparison between average strain results obtained using experimental and numerical analysis for (a) Case 1 at 10 kN, (b) Case 1 at 20kN, (c) Case 2 at 10 kN, (d) Case 3 at 20kN, (e) Case 3 at 5 kN, and (f) Case 3 at 8kN.

The finite element model was constructed in Abaqus analysis package. Core geometry was modelled as a 3D deformable solid mesh, composed of 20-node quadratic brick with reduced integration 3D stress elements (C3D20R). Element size was approximately 9 mm, found following a mesh convergence study. The boundary conditions at the base of both ends of the numerical model were fixed for all translational displacements. Restraint in the transverse direction (z-direction) was applied to core plates at the tab locations as shown in Figure 16a-b. A force-controlled reference point located at the top of the modelled specimen was used for load application in Case 1. Four force-controlled reference points located on the bottom of four steel shell elements were used for load application in Case 2. Case 3 was not modelled as no buckling occurred for this case. All longitudinal cores joints were attached together at the joint location using tie constraint elements, except for the middle joint in which a coupling constraint element was used to tie the top surface of the segments to an FRP shell element, composed of 4-node doubly curved thin shell with reduced integration and finite membrane strains (S4R) with 9mm mesh size.

Resulting buckling loads are plotted in Figure 17 and buckling modes for models with a 5 mm shift are shown in Figure 16c-d. It can be seen that from 0 to 4mm, arch buckling is not strongly affected by core misalignment. However, when the offset reaches 5mm, the buckling load reduces significantly. This offset corresponds to half of material thickness (4.5mm) which results in the centroid forces not falling within the cross-sectional geometric boundaries. For Case 1, a difference of 2.4% and 5.6% is seen between the buckling prediction and the experimental results of Arch 1 and 2, respectively. For Case 2, a difference of 5.1% is seen between the buckling prediction and experimental results for Arch 2. For both cases, the buckling mode can be seen to occur between lateral restraint provided by the inside face connections, so it can be concluded that geometric misalignment and inside face restraint locations are the major determining factors in the compressive buckling resistance of folded sandwich arches.

General static analysis was also carried out by applying the buckling load resulted from the linear buckling analysis for perfectly aligned cores. The resulted force-displacement curve plotted in Figure 14.

5.2. FRP layer fracture

Joint capacity as governed by FRP layer fracture can be estimated based on the theoretical maximum moment, obtained by substituting FRP strength

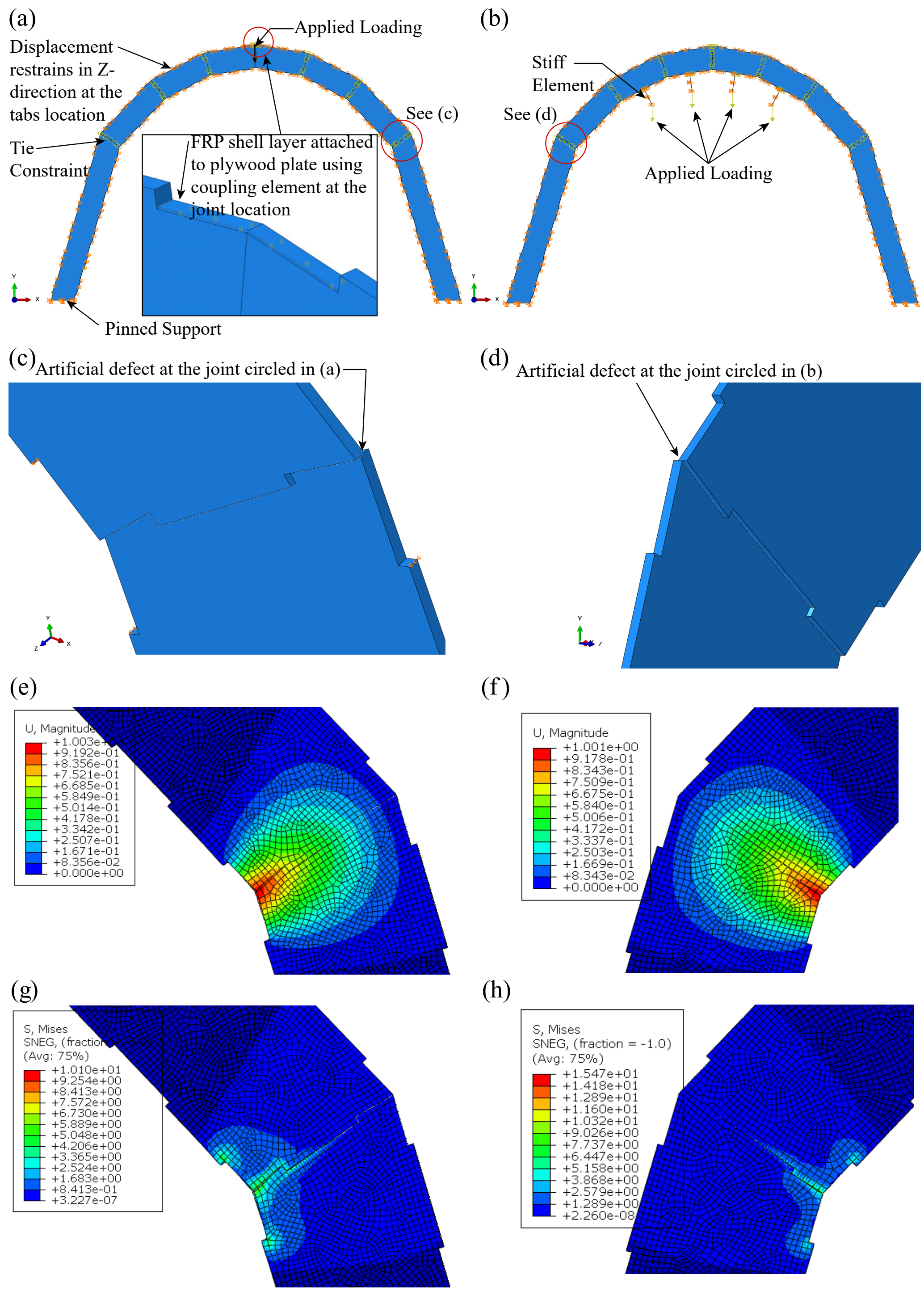

Figure 16: Numerical FE model definition for (a) Case 1 and (b) Case 2, artificial defect for (c) Case 1 and (d) Case 2, deformed shape at the first mode of failure for a single core arch with 5mm offset in the core segment for (e) Case 1 and (f) Case 2, and Mises stress distribution at the first mode of failure for a single core arch with 5mm offset in the core segment for (g) Case 1 and (h) Case 2.

values and joint load behaviour as per Figure 10c into Equation 2. This becomes:

$$M = f_t \times (t_f \times b) \times (d - \frac{c}{3} - \frac{t_f}{2}) \tag{7}$$

where f_t is the tensile strength of the FRP layer as per the experimental results of the direct material tensile testing, t_f is the FRP layer thickness (measured as 1.0mm), b is the width of the arch, d is the total section depth and c is the depth of the compression zone, obtained from DIC data as 60.3mm for Case 2 (also used for Case 1) and 109.1mm for Case 3. Of the complete set of FRP sample strength data as described in Supplementary Material S2, two FRP strength values were considered: the average strength from all material test speciments, 39.8MPa, and the minimum strength of any specimen, 33.8MPa. The minimum and average estimated moments for Case 1/2 were then 9.3 and 11.0kNm, respectively. The minimum and average estimated moments for Case 32 were 10.0 and 11.8kNm, respectively.

The estimated minimum and average moment capacity for each case is used to obtain the corresponding maximum applied load, P, from the numerical model with nonlinear hinges. The maximum load is obtained by increasing the load for each case until the predicted joint moment matches the theoretical capacity. The estimated applied load for each case calculated from the average and minimum moments are summarised in Table 4.

For Case 1, it can be noted that the experimental loading of the arch is

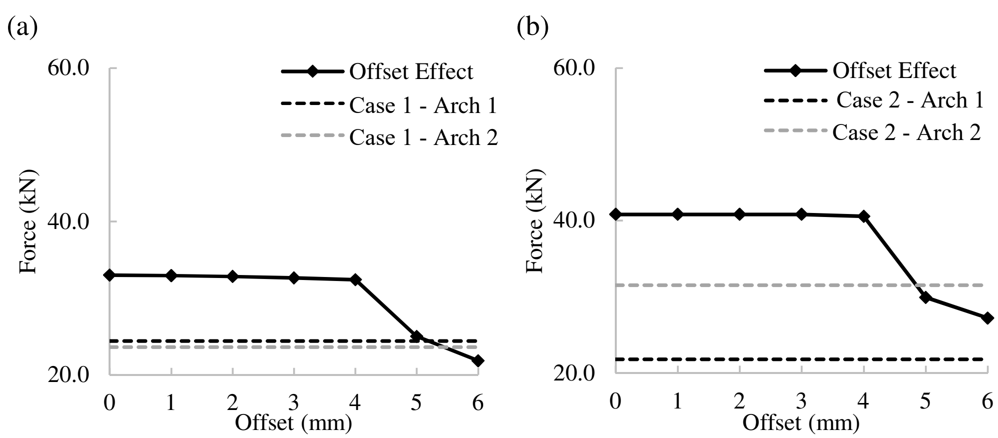

Figure 17: Critical buckling load versus first/last plate offset for (a) Case 1 and (b) Case 2.

bounded by the minimum and average predicted applied loading from FRP failure. Eccentric core local buckling is also within the FRP failure limit. For Case 2 Arch 2, the predicted applied loading is higher than the experimental value and the eccentric buckling load prediction, agreeing with the observed buckling failure behaviour. For Case 3, the minimum and average predicted applied loading from FRP failure bound the recorded experimental failure loads and match the FRP failure observed for both arches.

Table 4: Maximum applied load based on minimum and average FRP strength, and perfect or eccentric core plate alignment. All forces shown in kN.

Case	Arch No.	Failure mode	Exp. Force	FRP Strength		Buckling Strength	
				min.	avg.	perf.	ecc.
1	1	FRP fracture	24.4	*25.7*	*21.7*	-	-
	2	Plywood rupture	23.6	25.7	21.7	*33.0*	*23.1*
2	1	-	-	-	-	-	-
	2	Plywood rupture	31.5	43.7	37.0	*40.8*	*29.9*
3	1	FRP fracture	11.1	*13.4*	*11.0*	-	-
	2	FRP fracture	13.0	*13.4*	*11.0*	-	-

6. Discussion

The force-displacement behaviour of tested folded sandwich arches were successfully predicted using the simplified static non-linear analysis with extracted $M-\kappa$ hinge curves for most cases. A difference in structural stiffness prediction for Case 1 was attributed to the use of the $M-\kappa$ curve obtained for Case 2. It can be concluded that the joint rotational stiffness is a significant determining factor in the global strength and stiffness for folded sandwich structures.

Regarding load distribution, the rotational press fit joints behaved as predicted, with a hinge forming at location of peak sagging moment and load distributed to adjacent joints acting semi-rigidly under hogging moment. The strain distribution calculated from numerically-predicted joint moments matched the measured experimental strain distribution, again for all cases except for the middle joint of Case 1. This location corresponded to the loading point for that case, which may have influenced the strain gauge reading.

Joint locations with peak moment loads were seen to fail through either FRP layer tear out or longitudinal core buckling failures. For instances where FRP layer tear out governed, the tensile capacity of FRP layer could be used to predict a joint moment capacity and correspondingly predict a maximum applied numerical load, with good correspondence seen between predicted and experimental failure loads. For instances where core buckling governed, a numerical buckling analysis with a core misalignment defect was able to predict failure loads, with buckling length constrained by discrete lateral restraint at core-inside face tab locations.

The strength of folded sandwich systems can therefore be concluded as governed by RPF joint capacity, as limited by the tensile strength of the FRP layer or the precision of longitudinal alignment of core plates. With these insights, it is likely that further improvements can be made to the folded sandwich system to increase structural performance. Improvements to loading and restraint methods for experimental prototypes, and measurement of joint rotational stiffness for numerical model input, are likely to further improve the numerical modelling approach for system design.

7. Conclusion

This paper investigated the structural behaviour of folded sandwich structures assembled with rotational press-fit (RPF) integral joints and a hybrid FRP-timber material system. Key findings of the paper are summarised as:

- Structural load transfer occurs through semi-rigid joint behaviour in RPF joints acting under hogging moments, and hinge formation at RPF joints acting under sagging moments.

- The overall strength of the investigated folded sandwich arches is governed by the flexural strength (FRP tensile fracture and timber core plate compressive rupture) of the RPF joints.

- A simplified numerical 2D frame analysis was implemented with a bilinear semi-rigid joint stiffness obtained from experimental measurements. This gives a reasonable estimation of strength and a good prediction of the load distribution behaviour as measured by strain gauge instrumentation, but is highly sensitive to the joint $M - \kappa$ characterisation.

- Compressive force transfer occurred primarily through core plates, with no compressive strain measured through the bottom skin of the folded sandwich arches. However, the bottom skin is important for the lateral stability and alignment of the longitudinal cores, with compressive rupture failures found to occur from eccentric loading between misaligned sandwich segments.

Further work is needed to improve the precision and robustness of the joint rotational stiffness characterisation, as the current measurement gave different stiffness measurements from different tested load cases. Development of analytical or additional numerical tools for prediction of joint stiffness attributes would greatly assist this, by reducing the reliance on full-scale experimental testing. It would also allow for close study of the effect of particular joint parameters, for example plate thickness and tab length.

8. Acknowledgements

The corresponding author is grateful for the financial support provided by Australian Research Council Grant DE160100289. The first author would like to acknowledge the UQ Dow Centre for Sustainability Innovation Student Challenge Award in 2017. The authors would also like to give thanks to Dr Van Thuan Nguyen and Mr Christopher Russ for assistance in experimental testing.

References

[1] J. Song, Y. Chen, G. Lu, Axial crushing of thin-walled structures with origami patterns, Thin-Walled Structures 54 (2012) 65–71.

[2] J. Ma, Z. You, Energy absorption of thin-walled beams with a pre-folded origami pattern, Thin-Walled Structures 73 (2013) 198–206.

[3] A. Lebée, From folds to structures, a review, International journal of space structures 30 (2) (2015) 55–74.

[4] B. Xing, D. Hu, Y. Sun, J. Yang, T. Yu, Effects of hinges and deployment angle on the energy absorption characteristics of a single cell in a deployable energy absorber, Thin-Walled Structures 94 (2015) 107–119.

[5] T.-U. Lee, J. M. Gattas, Geometric design and construction of structurally stabilized accordion shelters, Journal of Mechanisms and Robotics 8 (3) (2016) 031009.

[6] K. B. Plasencia Alava, L. K. McCann, G. Hodge, K. Baber, J. M. Gattas, Computational design and experimental behaviour of deployable mass timber arches, Journal of the International Association for Shell and Spatial Structures 60 (1) (2019) 90–100.

[7] L. He, C. Liu, Z. Wu, J. Yuan, Stability analysis of an aluminum alloy assembly column in a modular support structure, Thin-Walled Structures 135 (2019) 548–559.

[8] J. D. van der Woerd, R. Chudoba, J. Hegger, Canopy–doubly curved folded plate structure, in: High Tech Concrete: Where Technology and Engineering Meet, Springer, 2018, pp. 2512–2520.

[9] J. Liu, H. Ou, R. Zeng, J. Zhou, K. Long, G. Wen, Y. M. Xie, Fabrication, dynamic properties and multi-objective optimization of a metal origami tube with miura sheets, Thin-Walled Structures 144 (2019) 106352.

[10] W. Du, Q. Liu, Z. Zhou, N. Uddin, Experimental investigation of innovative composite folded thin cylindrical concrete shell structures, Thin-Walled Structures 137 (2019) 224–230.

[11] O. D. Krieg, K. Dierichs, S. Reichert, T. Schwinn, A. Menges, Performative architectural morphology: Robotically manufactured biomimetic finger-joined plate structures (2011).

[12] J.-M. Li, J. Knippers, Pattern and form-their influence on segmental plate shells, in: Proceedings of IASS Annual Symposia, Vol. 2015, International Association for Shell and Spatial Structures (IASS), 2015, pp. 1–12.

[13] C. Robeller, A. Stitic, P. Mayencourt, Y. Weinand, Interlocking folded plate: Integrated mechanical attachment for structural wood panels, in: Advances in architectural geometry 2014, Springer, 2015, pp. 281–294.

[14] L. Chen, L. Sass, Fresh press modeler: A generative system for physically based low fidelity prototyping, Computers & Graphics 54 (2016) 157–165.

[15] Z. Su, L. Chen, X. He, F. Yang, L. Sass, Planar structures with automatically generated bevel joints, Computers & Graphics 72 (2018) 98–105.

[16] C. Robeller, Y. Weinand, Fabrication-aware design of timber folded plate shells with double through tenon joints, in: Robotic Fabrication in Architecture, Art and Design 2016, Springer, 2016, pp. 166–177.

[17] A. C. Nguyen, Y. Weinand, Development of a spring model for the structural analysis of a double-layered timber plate structure with through-tenon joints, in: World Conference on Timber Engineering (WCTE 2018), 2018.

[18] L. Sass, M. Botha, The instant house: a model of design production with digital fabrication, International Journal of Architectural Computing 4 (4) (2006) 109–123. doi:{10.1260/147807706779399015}.

[19] A. Stitic, C. Robeller, Y. Weinand, Experimental investigation of the influence of integral mechanical attachments on structural behaviour of timber folded surface structures, Thin-Walled Structures 122 (2018) 314–328.

[20] A. R. Rad, H. V. Burton, Y. Weinand, A new macro modeling approach in structural analysis of integrally-attached timber plate structures, CompWood (2019a) 26–26.

[21] P. Haller, Semi-rigid Timber Joints Structural Behaviour, Modelling and New Technologies: Final Report of Working Group," Timber Joints": Semi-rigid Behaviour of Civil Engineering Structural Connections: COST C1, European Commission, 1999.

[22] M. Dedijer, S. N. Roche, Y. Weinand, Shear resistance and failure modes of edgewise multiple tab-and-slot joint (mtsj) connection with dovetail design for thin lvl spruce plywood kerto-q panels, in: World conference on timber engineering, no. EPFL-CONF-221015, 2016.

[23] H. Buri, Y. Weinand, Origami-folded plate structures, architecture, Tech. rep. (2008).

[24] A. Stitic, Y. Weinand, Timber folded plate structures–topological and structural considerations, International Journal of Space Structures 30 (2) (2015) 169–177.

[25] S. Roche, C. Robeller, L. Humbert, Y. Weinand, On the semi-rigidity of dovetail joint for the joinery of lvl panels, European Journal of Wood and Wood Products 73 (5) (2015) 667–675.

[26] A. Stitic, A. C. Nguyen, A. Rezaei Rad, Y. Weinand, Numerical simulation of the semi-rigid behaviour of integrally attached timber folded surface structures, Buildings 9 (2) (2019) 55.

[27] S. Roche, G. Mattoni, Y. Weinand, Rotational stiffness at ridges of timber folded-plate structures, International Journal of Space Structures 30 (2) (2015) 153–167.

[28] J. Gamerro, I. Lemaıtre, Y. Weinand, Mechanical characterization of timber structural elements using integral mechanical attachments, in: 2018 World Conference on Timber Engineering (WCTE), 2018.

[29] A. C. Nguyen, J. Gamerro, J.-F. Bocquet, Y. Weinand, 3d finite element model for shear stiffness of wood-wood connections for engineered timber panels, CompWood (2019) 99–99.

[30] A. R. Rad, Y. Weinand, H. Burton, Experimental push-out investigation on the in-plane force-deformation behavior of integrally-attached timber through-tenon joints, Construction and Building Materials 215 (2019c) 925–940.

[31] C. Robeller, P. Mayencourt, Y. Weinand, Snap-fit joints-cnc fabricated, integrated mechanical attachment for structural wood panels, in: ACADIA 2014 Design Agency: Proceedings of the 34th Annual Conference of the Association for Computer Aided Design in Architecture, no. CONF, Riverside Architectural Press, 2014.

[32] C. Robeller, J. Gamerro, Y. Weinand, Théâtre vidy lausanne-a double-layered timber folded plate structure, Journal of the International Association for Shell and Spatial Structures 58 (EPFL-ARTICLE-233811) (2017) 295–314. doi:{10.20898/j.iass.2017.194.864}.

[33] C. Robeller, M. Konaković, M. Dedijer, M. Pauly, Y. Weinand, Double-layered timber plate shell, International Journal of Space Structures 32 (3-4) (2017) 160–175.

[34] A. R. Rad, H. Burton, Y. Weinand, Performance assessment of through-tenon timber joints under tension loads, Construction and Building Materials 207 (2019b) 706–721.

[35] Y. Al-Qaryouti, K. Baber, J. M. Gattas, Computational design and digital fabrication of folded timber sandwich structures, Automation in Construction 102 (2019) 27–44.

[36] Y. Alqaryouti, D. Fernando, J. Gattas, Structural behavior of digitally fabricated thin-walled timber columns, International Journal of Structural Stability and Dynamics 19 (10) (2019) 1950126.

[37] Z. Xin, J. Gattas, Structural behaviors of integrally-jointed plywood columns with knot defects, International Journal of Structural Stability and Dynamics (2020) 2150022.

[38] J. M. Gattas, M. L. O'Dwyer, M. T. Heitzmann, D. Fernando, J. Teng, Folded hybrid frp-timber sections: concept, geometric design and experimental behaviour, Thin-Walled Structures 122 (2018) 182–192.

[39] R. Park, T. Paulay, Reinforced concrete structures, John Wiley & Sons, 1975.

[40] N. Armouti, Earthquake Engineering: Theory and Implementation with the 2015 International Building Code, McGraw Hill Professional, 2015.

[41] C. Miao, Fibre reinforced polymer-timber veneer composite, the University of Queensland, not published (2019).

[42] R. C. Hibbeler, Statics and mechanics of materials, Pearson Higher Ed, 2013.

Structural Behaviour of Folded Timber Sandwich Structures: Supplementary Data

S1. Arch testing specimen description

The tested arch specimens were designed and fabricated using geometric design to fabrication workflow available in [35]. The arch tested specimen geometry and segment dimension and parameters are shown in Figure S1 and Table S1.

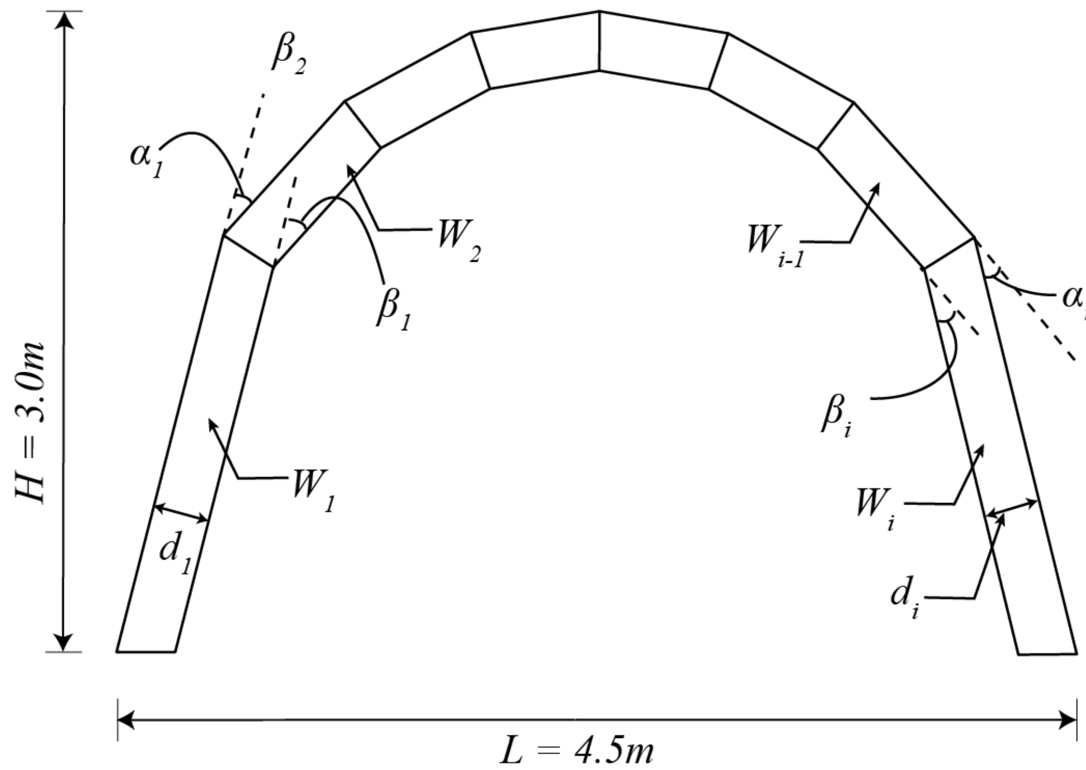

Figure S1. Arch specimen parameters description.

Table S1. Arch testing specimen parameters.

W_i	d_i (mm)	l_e (mm)	l_i (mm)	$\alpha_i = \beta_i$ (radians)
1	275	2026.7	1863.8	0.473
2	275	853.2	762.6	0.327
3	275	680.4	593.3	0.322
4	275	619.9	532.0	0.324
5	275	619.9	532.0	0.322
6	275	680.4	593.3	0.327
7	275	853.2	762.6	0.473
8	275	2026.7	1863.8	-

S2. Tensile test for FRP material

Tensile properties of the Biotex Flax 400g/m^2 2x2 Twill layer were obtained from testing conducted to ASTM D3500. Detailed dimensions of the specimens are as illustrated in Fig. S2a and the test setup is shown in Fig. S2b.

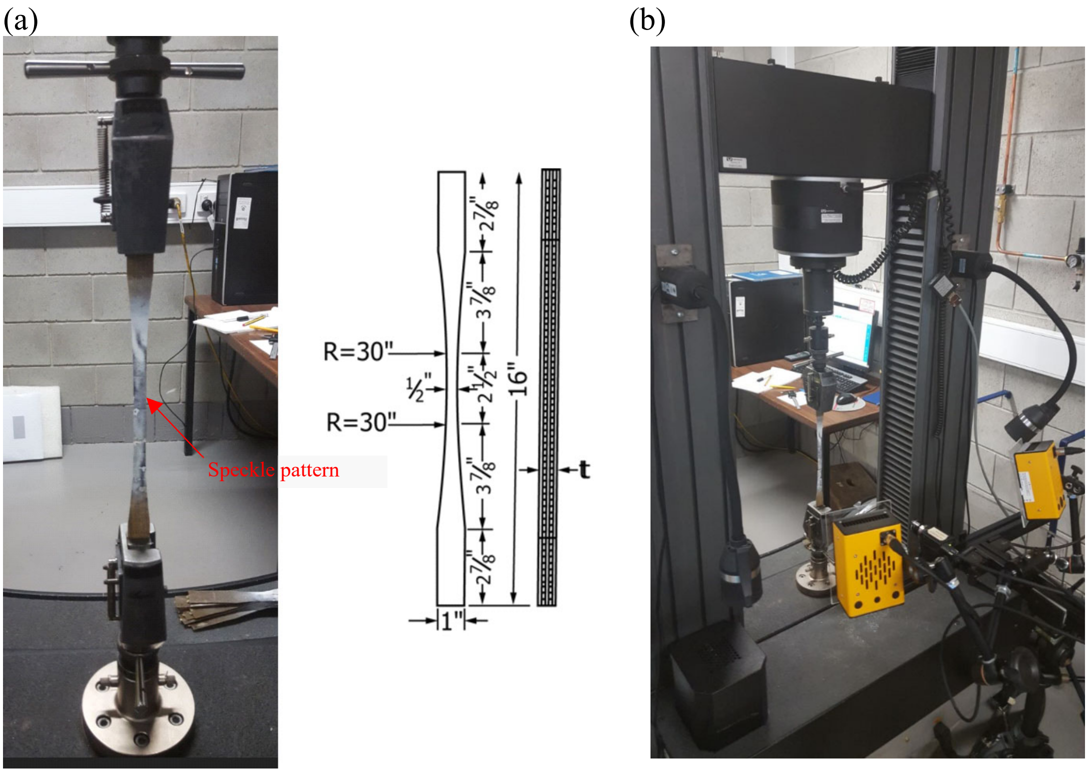

Figure S2. Material testing of FRP. (a) Sample dimensions and (b) test setup.

A displacement rate of 1.0mm/min was used for the test after initiation of loading as required by ASTM D3500. Specimens failed within 3-10 minutes and strain distribution during the test was captured by digital image camera (DIC).

Tensile strength was calculated as per the following equation proposed by ASTM D3039:

$$f_{tu} = \frac{P_{tu}}{\mathrm{A}}$$

Where P_{tu} is the maximum tension force obtained from the test and A is the cross-sectional area at the failure location. Specimen test results are summarised in Table S2.

Table S2. Tensile test results

Sample #	**A (mm^2)**	**P_{tu} (N)**	**F_{tu} (Mpa)**	**Average F_{tu} (Mpa)**	**E (MPa)**	**Average E (MPa)**
1	20.7	852.7	41.2	39.8	3740.1	3709.1
2	21.1	908.9	43.0		3865.4	

3	21.1	792.8	37.6		4241.5	
4	23.4	789.9	33.8		2610.0	
5	24.4	951.1	38.9		3761.0	
6	22.0	943.7	42.9		3775.8	
7	19.5	859.4	44.2		4376.4	
8	25.7	981.2	38.1		3455.5	
9	24.3	857.5	35.3		3154.3	
10	21.0	899.5	42.8		4110.9	

The axial strain distribution within the gauge length of a specimen as measured by DIC is shown in Fig. 9. When the strain data is extracted, a line (white line in Figure S3) was selected within the failure region for each specimen, the mean axial strain value in the line was extracted and used as the strain value.

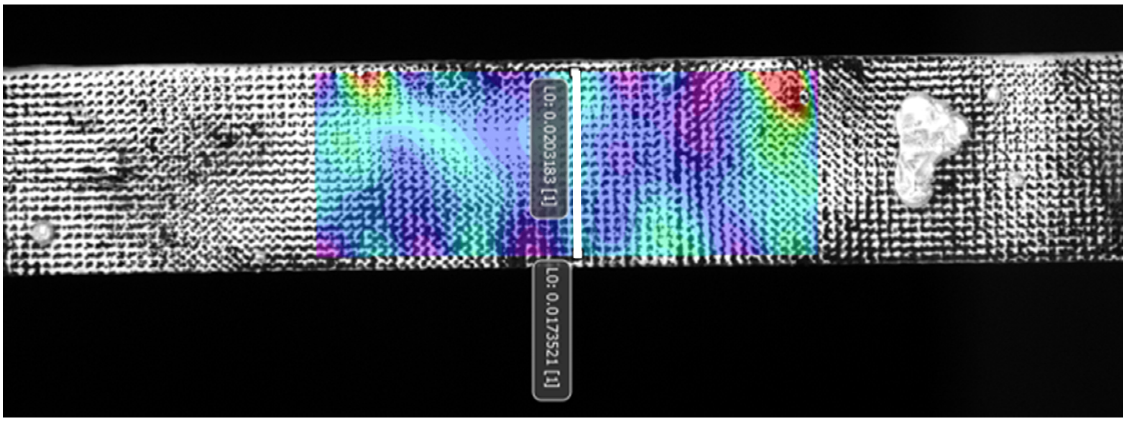

Figure S3: Strain distribution within the failure region of the tested specimen.

The stress-strain curves of the tested specimens are as shown in Fig. S4. The tensile modulus of FRP was calculated using the below equation, in which the stress is taken at two strain points at 1000 and 3000 μstrain according to ASTM D3039. The tensile modulus of the tested specimens are summarised in Table S1, where *E* is calculated as:

$$E = \frac{\Delta f}{\Delta \varepsilon}$$

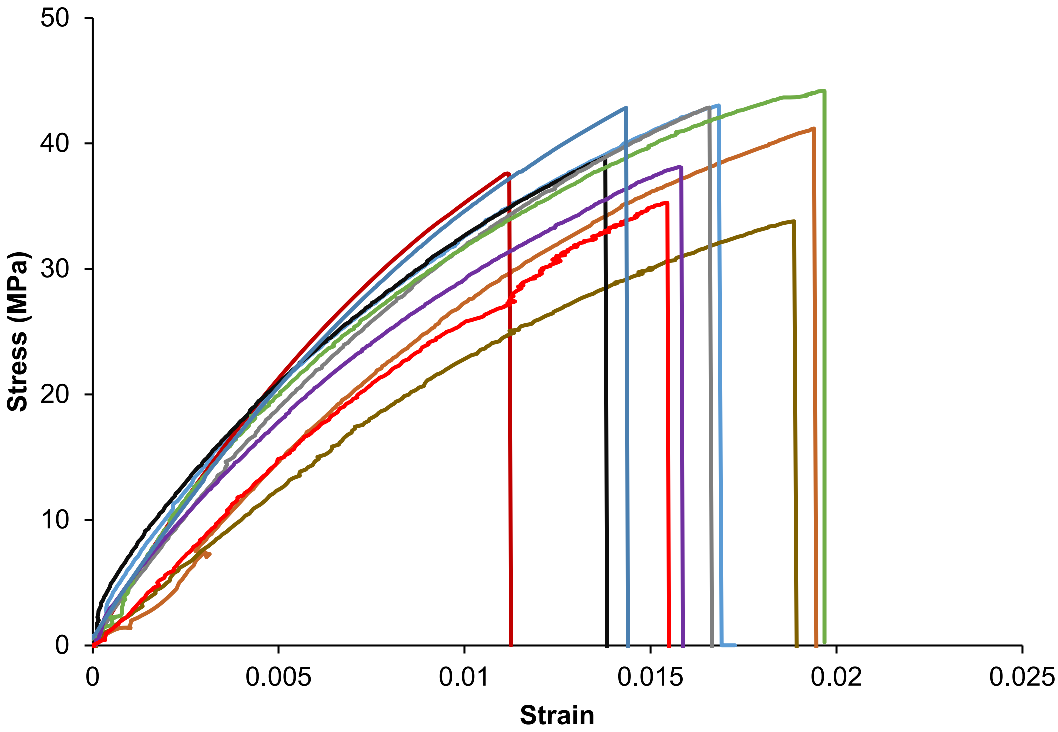

Figure S4: Stress-strain curve of the tested specimens.

S3. Plastic Hinge Length

The plastic hinge length which is used in the pushover analysis of the 2D frame model in SAP2000 was calculated in accordance with the below equation proposed in [39, 40]:

$$\frac{M_y}{M_u} = \frac{L_y}{L_y + L_p}$$

where M_y is the moment at the yielding point of the beam element, M_u is the ultimate moment, L_y is the length at the location of the yield moment and L_p is the plastic hinge length. Figure S5 shows the description of these parameters within a beam element.

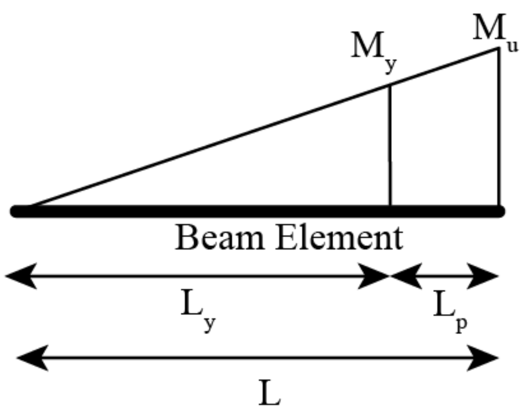

Figure S5: Description of plastic hinge parameters within a beam element.